

Exploring slip partitioning in the Southern Andes: New insights from fault slip data and crustal seismicity

José Cembrano¹, Alain Lavenu², Constanza Rojas³, Pablo Iturrieta⁴, Nicolás Pérez-Estay⁵, Ashley Stanton-Yonge⁶, Javiera Ruz-Ginouves⁷, Pamela Pérez-Flores⁸, Gerd Sielfeld⁹, Gabriela Zañartu¹, Rebecca Pearce¹⁰, Almudena Sánchez de la Muela¹¹, Tomás Roquer¹², Isabel Santibáñez¹³, Tiaren García¹⁴, Flavia Rojas¹⁵, Pablo Sánchez¹⁶, Simone Masoch^{6, 17}, Thomas Mitchell¹⁸, Gloria Arancibia¹, Ashley Griffith¹⁹, John Browning¹⁸, Karin Hofer²⁰, Gonzalo Yáñez¹

- (1) Departamento de Ingeniería Estructural y Geotécnica, Pontificia Universidad Católica de Chile Vicuña Mackenna 4860, Santiago, Chile, jcembrano@uc.cl, garancibia@uc.cl, gyaneza@uc.cl, gabrielazanartu@uc.cl
- (2) 10 rue de Cedres 64110, Gelos, France, alavenu2@orange.fr
- (3) Parcela 3, Camino El Yeco Tunquen, ruta F814, Algarrobo, Chile, corojas1@gmail.com
- (4) GFZ Helmholtz Centre for Geosciences, Potsdam, Germany, pciturri@gfz.de
- (5) Department of Earth Ocean and Atmospheric Science, University of British Columbia, Vancouver, Canada, nnperezestay@eoas.ubc.ca
- (6) Università degli Studi di Padova, Dipartimento di Geoscienze, Via Giovanni Gradeno, 6, 35131 Padova PD, Italia, ashley.sesnic.18@ucl.ac.uk
- (7) Department of Geology, University of Otago, 360 Leith Street, Dunedin, New Zealand, javiera.ruz@postgrad.otago.ac.nz
- (8) CIGEA (Consultoría Geológico Ambiental Ltda.), Manuel Rojas 23 Terrazas de Amancay, Huasco, Chile, pperezflores@gmail.com
- (9) University of Auckland, Faculty of Science, 23 Symonds Street 1010, Auckland, New Zealand gerd.sielfeld@auckland.ac.nz
- (10) Royal Roads University, Cascade Institute, 2005 Sooke Rd, Victoria, Canada. pearce@cascadeinstitute.org
- (11) Consejo Superior de Investigaciones Científicas, Instituto Geológico y Minero de España, Departamento de Riesgos Geológicos y Cambio Climático, Ríos Rosas 23, Madrid, España. asmgarzon@ucm.es
- (12) Departamento de Ingeniería de Minas, Metalurgia y Materiales, Universidad Técnica Federico Santa María, Av. Vicuña Mackenna 3939, Santiago, Chile. tomas.roquer@usm.cl
- (13) Las Hortensias 2546, Santiago, isantiboric@gmail.com
- (14) SRK Consulting Chile, Hydrogeology Area, Vitacura 2939, 9th floor, Santiago, Chile. tiaren.garcia@gmail.com
- (15) University of Manchester, Department of Earth and Environmental Sciences, Oxford Road M13 9PL, Manchester, UK. flavia.rojasguzman@manchester.ac.uk
- (16) Universidad Austral de Chile, Facultad de Ciencias, Avenida Rector Eduardo Morales Miranda s/n, Valdivia, Chile. pablo.sanchez@uach.cl
- (17) Nevada Seismological Laboratory, University of Nevada, Reno, USA. smasoch@unr.edu
- (18) University College London, Department of Earth Sciences, Gower Street, London, UK, Thomas Mitchell, j.browning@ucl.ac.uk
- (19) School of Earth Sciences, The Ohio State University, 43210, Columbus, Ohio, USA. griffith.233@osu.edu
- (20) Swiss Federal Institute of Technology in Lausanne (EPFL), Lausanne, Switzerland, karin.hoferapostolidis@epfl.ch

48 **Abstract**

49 Active slip partitioning between the subduction megathrust and the upper plate is
50 investigated in the oblique-convergence setting of the Nazca-South American plate
51 boundary between 33° and 47° S. This segment has two major along-strike bends:
52 the Maipo Orocline (~34° S) and the Arauco Peninsula (~38° S), whereas south of
53 38° S, lies the intra-arc Liquiñe-Ofqui Fault System (LOFS). Here we examine long-
54 and short-term upper-plate deformation by combining a harmonized catalog of about
55 2,300 fault-slip measurements in the forearc and arc regions, from which we derive
56 P-T axes using kinematic inversions, along with an integrated seismological
57 database for upper-plate events (1976-2025), including global and local networks.
58 These data are categorized by forearc, arc, and back-arc regions. We identify four
59 distinct tectonic segments based on the spatial distribution of P and T axes in the
60 long-and short-term: (1) 33°–34° S, showing both ~E–W and ~N–S subhorizontal
61 shortening in the forearc and arc areas, suggesting active radial shortening; (2) 34°–
62 37° S, dominated by mostly blind, seismogenic, margin-parallel dextral faults along
63 with NW- and NE-trending structures running at a high angle with respect to the plate
64 margin (called transverse faults here); (3) 37°–41° S, where margin-orthogonal
65 subhorizontal shortening in the submerged forearc coexists with nearly margin-
66 parallel shortening in the emerged forearc, with contemporaneous dextral slip along
67 the LOFS and ~E–W shortening accommodated by transverse NE-trending dextral
68 and NW-trending sinistral seismically active faults; and (4) 41°–47° S, a region
69 governed mainly by the geometry and kinematics of the LOFS strike-slip duplex.
70 Kinematic indicators on mesoscopic faults (mostly slickenfibers) and a lack of
71 pseudotachylytes suggest a considerable aseismic component to upper-plate fault
72 slip, implying that morphotectonic slip rates may overestimate seismic hazard.

73 Future detailed geodetic data may help better constrain the relative contributions of
74 aseismic and seismic slip on the upper-plate faults in this Andean segment.

75 **Resumen**

76 **Explorando la partición del deslizamiento en los Andes del Sur: Nuevas** 77 **perspectivas a partir de datos de deslizamiento de fallas y sismicidad cortical.**

78 La partición del vector de convergencia entre la zona de subducción y la placa
79 superior es analizada en el contexto de la convergencia oblicua entre las placas de
80 Nazca y Sudamérica, desde los 33° S hasta los 47° S. Este segmento presenta dos
81 marcadas curvaturas en el margen continental: el Oroclino de Maipo (~34° S) y la
82 Península de Arauco (~38° S), mientras que al sur de los 38° S se desarrolla, en el
83 dominio de intra-arco, el Sistema de Fallas Liquiñe-Ofqui (SFLO). En este trabajo se
84 examina la deformación de la placa superior mediante un catálogo de
85 aproximadamente 2.300 mediciones de fallas en las regiones del antearco y del
86 arco, junto con datos sismológicos de eventos entre 1976 y 2025, procedentes de
87 redes globales y locales, categorizados como de antearco, arco y trasarco. Se
88 identifican cuatro segmentos tectónicos con base en la distribución espacial de los
89 ejes P y T: (1) 33°–34° S, con acortamiento subhorizontal en direcciones ~E-O y ~N-
90 S, lo que sugiere acortamiento radial; (2) 34°–37° S, dominado por fallas dextrales,
91 en su mayoría ciegas, sismogénicas y paralelas a la margen, junto con estructuras
92 sismogénicas de rumbo NO y NE; (3) 37°–41° S, donde coexiste un acortamiento
93 ortogonal al margen en el antearco sumergido con otro paralelo al margen en el
94 antearco emergido. Adicionalmente, ocurren fallas transversales sísmicamente
95 activas, NO y NE, sinistral y dextrales, respectivamente; y (4) 41°–47°, una región
96 gobernada principalmente por la geometría y cinemática del SFLO. Indicadores

97 cinemáticos en fallas mesoscópicas (e.g., fibras de crecimiento) y la ausencia de
98 pseudotaquilitas sugieren una componente asísmica significativa, lo que puede
99 llevar a sobreestimar el peligro sísmico calculado mediante estimaciones
100 morfotectónicas. Futura información geodésica de detalle puede contribuir a
101 discriminar de mejor manera el deslizamiento sísmico del asísmico en las fallas de
102 la placa superior de este segmento de los Andes.

103 **INTRODUCTION**

104 The partitioning of upper plate deformation at obliquely convergent margins has
105 been studied for over fifty years (e.g., Fitch, 1972; Jarrard, 1986; Beck, 1991;
106 McCaffrey, 1992, 1996; Canora et al., 2014; Stanton-Yonge et al., 2016). Early
107 research by Fitch (1972) proposed that the oblique convergence vector is partitioned
108 into margin-orthogonal and margin-parallel slip components, with the former mainly
109 accommodated by the subduction zone and the latter by an intra-arc strike-slip fault
110 system within the upper plate. Beck (1991) and McCaffrey (1992) provided important
111 insights by suggesting that most obliquely convergent margins only show partial slip
112 partitioning, where only part of the oblique convergence is absorbed by oblique
113 displacement at the plate boundary, leading to a smaller residual margin-parallel slip
114 vector than otherwise assumed in earlier studies. Some years later, de Saint
115 Blanquat et al. (1998) refined earlier deformation and slip partitioning models by
116 proposing a conceptual framework for transpressional magmatic arcs as a general
117 model for obliquely convergent margins (Teyssier et al., 1995). In their model, they
118 define margin-parallel domains in the upper plate that accommodate not only one
119 component of the convergence vector but different degrees and combinations of
120 strike-slip and shortening deformation (Fig. 1). This framework was further improved

121 and applied to the specific case of the Southern Andes by Lavenu and Cembrano
122 (1999).

123 Recent seismological studies in the Chilean margin have suggested that the
124 accommodation of the margin-parallel component of the plate convergence vector
125 within the upper plate is more complex than previously understood (e.g., Sielfeld et
126 al., 2019a; Pérez-Estay et al., 2020). These studies revealed significant variations in
127 earthquake focal mechanisms within the brittle crust of the continental plate, in both
128 kinematics and orientations. Structural geology studies have independently reported
129 similar behavior in the long-term deformation recorded in exhumed faults, suggesting
130 that the margin-parallel component is accommodated by numerous reactivated and
131 new faults with varying strike, dip, and kinematics, many of which show evidence of
132 activity from the Pliocene to the Quaternary (Pérez-Flores et al., 2016; Sielfeld et al.,
133 2017). Numerical models support these field observations, highlighting the
134 importance of fault strike relative to the margin and showing that a range of fault
135 kinematics can coexist to accommodate the margin-parallel slip component
136 (Stanton-Yonge et al., 2016). Analog models of the Southern Andean oblique
137 subduction plate margin are consistent with these observations as well (e.g.,
138 Eisermann et al., 2021).

139 Overall, evidence from seismology, structural geology, and numerical modeling
140 suggests that slip complexity involves not only margin-parallel faults but also
141 transverse faults, which significantly contribute to accommodating fault slip in the
142 upper plate. In this study, we present a review of the existing published
143 seismological and field structural data for the Southern Andes between 33° and 47°
144 S, a segment marked by the end of flat subduction in the north (e.g., Jordan et al.

145 1983) and the Chile Triple Junction in the south (e.g., Forsythe and Nelson, 1985).
146 This continental segment features two sharp inflections of the plate margin, one at
147 $\sim 34^\circ$ S (Maipo Orocline) and another around 38° S (Arauco Peninsula) (Fig. 2).
148 Notably, two significant earthquake rupture zones associated with subduction
149 megathrust earthquakes overlap at the Arauco Peninsula: the 2010 Maule
150 earthquake and the 1960 Valdivia earthquake (e.g., Moreno et al., 2009, 2012; Vigny
151 et al., 2011). This latter region therefore represents a critical tectonic element of the
152 plate margin (e.g., Melnick et al., 2009), marking a slight but significant change in
153 plate obliquity (e.g., Stanton-Yonge et al., 2016) (Fig. 2).

154 In this manuscript, we aim to improve our understanding of how deformation and slip
155 resulting from oblique plate convergence are accommodated in the upper plate. Our
156 newly integrated structural and seismological evidence strongly suggests the
157 existence of four consecutive Andean segments that have experienced unique
158 tectonic evolution since the Neogene. This segmentation offers important insights
159 into the fundamental mechanisms underlying plate margin deformation and the
160 seismic hazards (and possible risks) associated with potentially seismogenic faults.

161 **2. TECTONIC AND GEOLOGICAL SETTING**

162 **2.1. Geology and crustal structure of the Southern Andes**

163 The Andean mountain range between 33° and 47° S shows a slightly deformed,
164 rigid, and cold forearc region adjacent to a weaker and hotter magmatic arc domain
165 (e.g., Tassara and Yáñez, 2003; Fariás et al., 2006; Cembrano and Lara, 2009;
166 Gerbault et al., 2009). This segment is characterized by a slightly dextral-oblique
167 convergence between the Nazca and South American plates, occurring at a rate of
168 approximately 7 cm/year (e.g., Angermann et al.; 1999; Quiero et al., 2022). Oblique

169 convergence has been dominant at the plate margin for the past ~20 Myr (Pardo-
170 Casas and Molnar, 1987; Somoza, 1998), with slight transient variations in the
171 obliquity angle ($<10^\circ$) on timescales of a few Myr (Quiero et al., 2022). The southern
172 boundary of the study region is defined by the Chile Triple Junction, where the active
173 Chile Ridge, which separates the Nazca plate from the Antarctic plate, is subducted
174 beneath the continent (Figs. 2 and 3).

175 The regional geological units between 33° and 47° S form belts roughly parallel to
176 the margin, from Paleozoic plutonic, volcano-sedimentary, and metamorphic rocks in
177 the forearc to Meso-Cenozoic plutonic and volcano-sedimentary formations in the
178 arc and back-arc regions (Fig. 2). In between, scattered outcrops of Oligocene-
179 Miocene rocks, predominantly obscured by more recent volcano-sedimentary
180 deposits, are present (Fig. 2).

181 Between 33° and 38° S, the basement rock units of the volcanic arc consist primarily
182 of extensive outcrops of Meso-Cenozoic volcanic and volcano-sedimentary rocks,
183 locally intruded by Neogene plutons (e.g., Charrier et al., 2002; Farías, et al., 2007;
184 Piquer et al., 2010; Pearce et al., 2020) (Fig. 2). This setting dramatically changes
185 south of $\sim 38^\circ$ S, where volcanoes are mostly constructed directly on top of Meso-
186 Cenozoic plutonic rocks (Hervé et al. 1994; Stern et al. 2011) (Fig. 2). Consistently,
187 Cenozoic regional exhumation rates, determined using both apatite and zircon
188 fission track data along the main range, show a sharp increase at around 38° S.
189 There, exhumation rates jump from <0.1 mm/year in the north to >1 mm/year to the
190 south (e.g., Thompson, 2002; Glodny et al., 2008).

191 Moreover, the crustal thickness beneath the magmatic arc steadily decreases from
192 approximately 55 km at 33° S to 35 km at 46° S, paralleled by a decline in the

193 average elevation of the Main Cordillera, from 5,000 m to under 2,000 m (Tassara
194 and Yáñez, 2003; Cembrano and Lara, 2009).

195 **2.2. Short-term slip partitioning**

196 To characterize the short-term crustal deformation between 33° and 47° S, we
197 compiled a comprehensive focal-mechanism catalog of $M_w > 5.0$ earthquakes in the
198 upper plate, spanning the entire forearc, arc and back-arc regions (Fig. 2). Compiled
199 from global network sources, the catalog aims to provide a present-day snapshot of
200 the state of stress and slip partitioning along and across the plate boundary.
201 Relevant ($M_w > 7.0$) subduction earthquakes were also recorded (Stanton-Yonge et
202 al., 2016), enabling the calculation of the margin-parallel component of oblique
203 subduction and its variation along strike (Fig. 2).

204 The dataset was constructed by integrating focal-mechanism solutions from the
205 Global Centroid Moment Tensor (GCMT; Ekström et al., 2012) and the Advanced
206 National Seismic System Comprehensive Catalog (ANSS-ComCat; U.S. Geological
207 Survey, 2017), harmonizing them into a unified format and retaining events within the
208 study area from 1976 to 2025. Events were filtered, merged, and checked for
209 duplicates (e.g., Weatherill et al., 2016), and supplemented with relocated
210 hypocenters where available (Potin et al., 2025). Using slab interface geometry
211 (Hayes et al., 2018) and kinematic criteria similar to those applied in the New
212 Zealand Seismic Hazard Model (e.g., Gerstenberger et al., 2024), we classified
213 events into forearc, intra-arc, and back-arc domains. The classification criteria and
214 the full catalog, further divided into intra-slab, outer-rise, and deep earthquakes, are
215 detailed in figure S1 of the Supplementary Material. The P- and T-axes of
216 earthquakes for each class are shown in figure S2 of the Supplementary Material.

217 More information regarding data processing and accessibility is provided in the Data
218 and Resources chapter at the end of this manuscript.

219 The seismicity related to the subduction interface exhibits reverse-slip and involves
220 ~N–S striking nodal planes with P-axes trending nearly E–W (Fig. 2). This indicates
221 a P-axis direction slightly rotated clockwise (~10-20°) from the plate margin slip
222 vector (Stanton-Yonge et al., 2016).

223 In the submerged forearc (west of the coastline), the seismicity is focused in the
224 rupture zones of the Mw 8.8 2010 Maule and Mw 8.0 1985 Valparaíso earthquakes
225 (Fig. 2). Most of these events (41 out of 49; ~84%) are aftershocks of the 2010
226 megathrust earthquake, and can be grouped into three populations: (1) 37 reverse-
227 slip events with nodal planes striking near N–S and P-axes trending close to E-W,
228 similar to the subduction-related events; (2) nine normal-slip events with nodal
229 planes striking NW, NS, and NE; and (3) three strike-slip events with margin-oblique
230 nodal planes and P-axes trending NE (Fig. 2).

231 In the emerged forearc (east of the coastline), 23 earthquakes (12 of which occurred
232 before the 2010 Maule earthquake) can be grouped as follows: (1) 11 with margin-
233 oblique nodal planes along the entire margin, either with strike-slip (three),
234 reverse/strike-slip (six), or normal/strike-slip (two) kinematics, exhibiting margin-
235 subparallel P-axes trending from N–S to NE; (2) six normal-slip earthquakes with
236 nodal planes striking near NW and near N–S, five of which are associated with the
237 Mw 6.9 2010 Pichilemu aftershock sequence (e.g., Aron et al., 2013); and (3) six
238 reverse-slip events with nodal planes striking mainly N–S (Fig. 2).

239 Intra-arc seismicity (28 events) is primarily represented by strike-slip events (Fig. 2),
240 with two exceptions: the normal, dip-slip, Mw 6.1 2007 Aysén earthquake, located at

241 45.4° S (Legrand et al., 2011), and three reverse-slip earthquakes at 34°, 35°, and
242 42° S. In the northern part of the study region, between 33° and 34° S, strike-slip
243 events have a nearly E–W oriented horizontal P-axis, with NW- and NE-striking
244 nodal planes, exhibiting sinistral or dextral kinematics, respectively. Between 34° and
245 37° S, earthquakes show strike-slip kinematics with subvertical nodal planes striking
246 approximately N25°E (dextral) and N65°W (sinistral). South of 37° S, the events
247 show strike-slip kinematics, with nodal planes striking between N20°W and N30°E,
248 mostly oriented from N–S to N10°E. Earthquake kinematics within the southern part
249 of the arc maintain a consistent orientation, characterized by a subhorizontal, NE-
250 trending P-axes, as also documented by local seismological networks (Lange et al.,
251 2008; Pérez-Estay et al., 2020).

252 **2.3. Long-term slip partitioning**

253 The long-term regional-scale structure of the intra-arc and back-arc domains
254 between 33° and 35° S is defined by east-verging, margin-parallel folds and thrusts
255 of Cenozoic age, representing the westernmost part of the Aconcagua and Malargüe
256 foreland fold-and-thrust belts (e.g., Giambiagi and Ramos, 2002). Major regional
257 reverse faults affect the Meso-Cenozoic volcano-sedimentary units, accommodating
258 a limited degree of shortening compared to the Andes of northern Chile (Giambiagi
259 et al., 2012). A similar intra-arc compression regime has been seismically recorded
260 in the 33°-34° S latitude range (Ammirati et al., 2022).

261 Available fault-slip data document the long-term stress and strain state of the forearc
262 and intra-arc regions since the Pliocene, revealing a local margin-parallel shortening
263 in the forearc and a NE-trending, subhorizontal maximum compression axis (σ_1)
264 across the volcanic arc, the latter prevalent from 37° to 46° S (e.g., Arancibia et al.,

265 1999; Lavenu and Cembrano, 1999; Cembrano et al., 2000; Lara et al., 2006). In the
266 arc domain, the main compressional stress axis aligns with many volcanic features
267 and dike trends (Cembrano and Lara, 2009; Sielfeld et al., 2017), a pattern that is
268 also consistent with contemporaneous margin-parallel dextral strike-slip deformation.

269 Although margin-parallel reverse faults dominate, there is evidence of conjugate NE-
270 striking dextral and NW-striking sinistral strike-slip faults in the forearc (Aron et al.,
271 2013; Santibáñez et al., 2019), the magmatic arc (e.g., Rivera and Cembrano, 2000;
272 Piquer et al., 2015, 2021), and the foreland (Mescua et al., 2019; Olivar et al., 2022).
273 The major earthquakes recorded between 34–37° S ($M_w > 6$), namely the M_w 6.5
274 2004 Teno and the M_w 6.0 2012 El Melado, have strike-slip focal mechanisms,
275 confirming the seismogenic nature of the NE- and NW-trending faults in this area
276 (e.g., Sielfeld et al., 2019b). Moreover, these arc-oblique fault systems have been
277 proposed as structural controls on magmatism and mineralization (e.g., Piquer et al.,
278 2015).

279 Between 36° and 38° S, the Argentine foreland is characterized by the Neogene
280 Chos-Malal and El Agrio fold-and-thrust belts (e.g., Folguera et al., 2004, 2007), with
281 active back-arc volcanism coeval with E-W compression along the El Agrio belt (e.g.,
282 Galland et al., 2007). In contrast, the arc region, which lies within a fairly similar
283 latitude range, has undergone arc-orthogonal extension during the Quaternary,
284 accompanied by a minor component of dextral strike-slip displacement (Melnick et
285 al., 2006).

286 West of the El Agrio lies the Antifñir-Copahue fault zone, an east-vergent, high-angle
287 fault system characterized by dextral transpressive and dextral transtensive faults,
288 which forms the orogenic front at these latitudes (Folguera et al., 2004). This fault

289 zone merges southwestwards with the 1200 km-long Liquiñe-Ofqui Fault System
290 (LOFS), a major intra-arc fault system that extends from 38° to 47° S (Hervé, M.,
291 1976; Hervé et al., 1979; Hervé, 1994; Cembrano et al., 1996; Folguera et al., 2002;
292 Rosenau et al., 2006; Pérez-Flores et al., 2016; Sielfeld et al., 2019a). Evidence
293 from ductile-to-brittle shear zones suggests that the LOFS has been active as a
294 transpressional dextral strike-slip structure for at least the past 6 Myr (Arancibia et
295 al., 1999; Cembrano et al., 2002), and that it may have acted as a leaky transform
296 fault ~25 Ma ago (Hervé et al., 1995). This fault was believed to be spatially and
297 genetically linked to sedimentation, local magma ascent, and concomitant pillow lava
298 formation under a deep-rooted transtensional regime (Hervé et al., 1995). The
299 shortening component of Pliocene-to-recent intra-arc deformation increases to the
300 south as the LOFS approaches the Chile Triple Junction (e.g., Lavenu and
301 Cembrano, 1999; Cembrano et al., 2002; Thompson, 2002; Rosenau et al., 2006).

302 In the study area, a landmark paper providing an overview of different stress states
303 associated with individual volcanoes is that of Pérez-Estay et al. (2023). The study
304 used available fault-slip data and earthquake focal mechanisms to classify volcanoes
305 by their stress states. A key conclusion is that the stress regime along the arc is
306 neither uniform nor of a single type; instead, it exhibits a spatial and/or temporal
307 coexistence of distinct and even opposing stress regimes, a pattern also recognized
308 in previous studies, albeit at more local scales (e.g. Pérez-Flores et al., 2016). The
309 most frequently observed regime corresponds to the one initially identified at the
310 regional scale: a strike-slip regime with σ_1 and σ_3 orientated NE and NW,
311 respectively. Additionally, a localized stress regime with a vertical σ_1 has been
312 systematically observed in several large volcanoes, likely resulting from transient
313 stress rotation driven by magma pressure (Pérez-Estay et al., 2023).

314 3. METHODS AND RESULTS

315 3.1. Long-term deformation: fault slip data from crustal faults, a harmonized 316 new compilation.

317 Over the past 15 years, the quantity and quality of fault-slip data collected in the
318 field, particularly in the volcanic arc region, have significantly improved, yielding new
319 insights into Pliocene and younger slip partitioning and the regional and local
320 strain/stress states (Sánchez et al., 2013; Pérez-Flores et al., 2016; Sielfeld et al.,
321 2019a, b; Ruz-Ginouves et al., 2020; Mura et al., 2025). Figure 3 presents a
322 summary of all the data collected from structural sites mapped by our research group
323 since the early 1990s (see the Data and Resources chapter at the end of this
324 manuscript for the complete dataset). We deliberately included only results from our
325 group because the conceptual approach and field methodology have been applied
326 consistently, using the same geological and structural criteria to define the geometry
327 and kinematics of mesoscopic faults (see, for instance, Pérez-Flores et al., 2016). In
328 the Discussion section these results are placed into a broader literature context.

329 Our compilation includes around 2,300 mesoscopic fault surfaces, for which we
330 recorded the strike, dip, and rake of the striae. These faults affect Cretaceous to
331 recent rock units, although only those that are clearly post-Miocene were considered
332 in the analysis of current slip partitioning because the plate convergence vector, as
333 stated earlier, has remained nearly constant in magnitude and direction over the past
334 20 Myr. Faults affecting Cretaceous and Paleogene rock units in the forearc are
335 presented to account for earlier deformation patterns expected to differ from those of
336 neotectonic activity.

337 Faults were identified and measured along the master and subsidiary faults of the
338 LOFS, along NW- and WNW-striking transverse faults in the intra-arc, and at five
339 sites in the forearc (Fig. 3). Fault displacement sense was determined by examining
340 key features on the fault planes, including secondary fractures, mineral
341 crystallization, and tension cracks, among other kinematic indicators (e.g., Petit,
342 1987). The orientations of the maximum shortening (P) and maximum stretching (T)
343 instantaneous axes for each fault plane were obtained through FaultKin v.7.4.1
344 (Marrett and Allmendinger, 1990; Allmendinger et al., 2012), based on the fault
345 plane's orientation and the resolved displacement vector (slickenline). The
346 representative orientations of the P and T axes for a fault population were calculated
347 under the assumption of small single displacements and a consistent deformation
348 field, by assuming a statistical Bingham distribution. Non-clustered P- and/or T-axes
349 suggest kinematic heterogeneity in faulting, which may be caused by factors such as
350 triaxial deformation or reactivation of anisotropies. Neighboring sites with consistent
351 P–T results were grouped to make the data easier to understand and visualize,
352 obtaining 18 clusters (Fig. 3). In eight of these (Farellones, Maipo, Teniente, Teno,
353 Maule, Lonquimay, Ranco, and Puyuhuapi), more than one solution was identified,
354 resulting in two to four P–T axis stereoplots (Fig. 3). As we focus on deformation and
355 slip partitioning rather than stress fields, we chose to present the data in a manner
356 that reflects observations with minimal interpretation, consciously avoiding stress
357 inversion programs. For the interested reader, stress field analyses conducted for
358 the study area can be found in Arancibia et al. (1999), Cembrano and Lara (2009),
359 Pérez-Flores et al. (2016), Sielfeld et al. (2019b), and Pérez-Estay et al. (2023),
360 among others.

361 Overall, regional-scale analysis of the P-T axes from fault slip data in the volcanic
362 arc indicates two primary maximum shortening axes: one oriented N60°E and the
363 other trending ~E-W. In both cases, the minimum shortening axis is predominantly
364 horizontal. When analyzed in greater detail, the following is recognized (Fig. 3):

365 (1) Sites in the forearc between 33° and 34° S were mapped in Cretaceous rock
366 units (Colliguay), while those in Rapel and San Antonio affect Neogene
367 sedimentary rocks. Although these sites exhibit a high dispersion in kinematic
368 axis solutions, both P and T axes are predominantly subhorizontal, with roughly
369 E-W shortening in clusters Colliguay and Rapel. North of 34° S, sites San
370 Antonio, Farellones, and Maipo display a margin-parallel shortening. Sites at
371 Farellones cut Miocene rock units, whereas those at Maipo affect Quaternary
372 strata (Lavenu and Cembrano, 2008). Clusters Pelequén and Los Andes show a
373 higher dispersion in the kinematic axis solutions, but a general NE-trending
374 horizontal P-axis and a NW-trending subhorizontal T-axis. Faults at these sites
375 affect Cretaceous to Miocene rock units.

376 (2) In the volcanic arc north of 34.5° S, a subhorizontal, roughly E–W shortening
377 is also present, as documented at sites Farellones and Maipo. At these sites,
378 extension axes are predominantly subhorizontal to horizontal, whereas at
379 Teniente, just west of the volcanic arc, horizontal N–S shortening is documented.
380 Faults at Teniente cut Pliocene rock units.

381 (3) Farther south, in the Main Cordillera at the Teno site (~35°S), the P-axis
382 solution remains ~E–W, with both P and T subhorizontal. This solution is
383 compatible with the dominant NE-dextral and NW-sinistral strike-slip faults

384 observed in the field. Most of these faults are no older than Oligocene or
385 Miocene.

386 (4) At around 36° S, sites within the intra-arc area (Maule site) were mainly
387 mapped in Oligocene to Pleistocene volcano-sedimentary rocks. Fault-slip
388 analysis reveals three distinct orientations of the P-T axis. The first features a
389 horizontal NE-trending P-axis that aligns with the regional ~N60°E maximum
390 shortening direction. The second displays a horizontal P-axis rotated to N60°W.
391 However, the most prevalent orientation is characterized by a nearly vertical P-
392 axis and a N-S trending T-axis, compatible with E-W striking Pliocene–
393 Pleistocene normal faults.

394 (5) In the forearc at 38° S (Esperanza site), faults that displace Quaternary
395 sedimentary rocks (Lavenu and Cembrano, 1999) show a horizontal N–S
396 trending P-axis with a near-vertical T-axis.

397 (6) Between 38° and 42° S, all clusters within the intra-arc domain exhibit a
398 horizontal to slightly plunging NE-trending P-axis and a horizontal to slightly
399 inclined NW to NNW-trending T-axis. Some individual sites at Lonquimay and
400 Ralco show a slight clockwise rotation of both P- and T-axes towards E–W and
401 N–S trends, respectively. The maximum age of the mapped faults is Miocene.

402 (7) Near the southern end of the study area (~44.5° S), the Puyuhuapi cluster
403 represents faults affecting Miocene and Pliocene rock units. Fault-slip analysis
404 indicates two main kinematic axis solutions: one with a horizontal-to-
405 subhorizontal NE-trending P-axis and a horizontal-to-subhorizontal NW-trending
406 T-axis, and another showing clockwise rotation of both P- and T-axes toward E-
407 W and N-S, respectively.

408 **3.2 Short-term deformation: integrated seismological data from crustal**
409 **earthquakes from local networks**

410 The availability of seismological data from crustal faults in the southern Andes has
411 significantly increased both in quantity and quality over the past two decades (e.g.,
412 Lange et al., 2008; Mora et al., 2010; Legrand et al., 2011; Agurto et al., 2012;
413 Sielfeld et al., 2019a). This has been possible thanks to the deployment of local
414 networks focused on current deformation processes and stress state, particularly for
415 the arc and forearc regions (e.g., Farías et al., 2011; Ammirati et al., 2019; Pearce et
416 al., 2020; Pérez-Estay et al., 2020; Stanton-Yonge et al., 2025). These
417 developments have also enabled the identification of seismogenic faults within
418 known regional-scale fault systems and the potential discovery of unknown
419 concealed faults. Previously, seismic data were mostly accessible only through the
420 U.S. Geological Survey global seismological network, with a few exceptions noted in
421 local studies (Barrientos and Acevedo, 1992).

422 We compiled focal mechanisms of seismic activity detected by temporary local
423 networks in and next to the volcanic arc domain (Fig. 4), reported on previously
424 published studies (Lange et al., 2008; Mora et al., 2010; Agurto et al., 2014;
425 Ammirati et al., 2019; Sielfeld et al., 2019a; Pérez-Estay et al., 2020; Montenegro et
426 al., 2021; Mura et al., 2025; Stanton-Yonge et al., 2025) to examine the current
427 deformation processes occurring in the overriding plate. Due to variability in
428 magnitudes, azimuthal gaps, and the number of observations at each source, all
429 mechanisms were included, as each dataset comes from a previously validated and
430 published study.

431 Figure 4d displays the distribution of P–T axes of focal mechanisms identified, along
432 with the number of mechanisms per network. We selected three regions covered by
433 one or more local networks to examine the spatial distribution of microseismicity and
434 crustal faults: Maipo (Ammirati et al., 2019; Fig. 4A), Araucanía (Sielfeld et al., 2019;
435 Montenegro et al., 2021) (Fig. 4B), and Aysén (Mora et al., 2010; Agurto et al., 2014;
436 Pérez-Estay et al., 2020) (Fig. 4C). The seismicity detected by the local networks is
437 shown as green dots and ranked by depth, along with a representative subset of
438 focal mechanisms from each network (full focal mechanisms database available in
439 the original references or in the Data and Resources chapter). A detailed discussion
440 about seismicity rates in each region is beyond the scope of this work. Instead, the
441 figures highlight the overall deformation pattern of the upper plate, as reflected in the
442 orientations and distributions of the P and T axes.

443 The reported seismicity generally covers relatively short time windows (typically
444 between 1 and 3 years of observation) and includes only events with $M_w < 5.0$. Thus,
445 it provides only a partial view of the ongoing processes and does not necessarily
446 represent the activity of major faults. Nevertheless, this information is valuable
447 because: (1) it allows spatial comparison between mapped faults and small
448 earthquakes, and (2) the high density of local stations makes it possible to estimate
449 focal mechanisms of small events that are not included in global catalogs. As our
450 results focus on seismic network deployments within and around the volcanic arc
451 domain, there is an inherent bias toward detecting higher seismicity rates in the arc
452 than in the forearc. However, the global compilation presented in figure 2 partly
453 compensates for this gap.

454 In figure 4, the current kinematics in the forearc and arc regions are evidenced by
455 numerous shallow crustal earthquakes of relatively small magnitude. The
456 orientations of P-T axes from focal mechanisms indicate a variety of fault kinematics.
457 The main observations are:

458 (1) Strike-slip focal mechanism solutions primarily characterize the arc region
459 between 34° and 47° S, with isolated normal events and even fewer reverse
460 events (e.g., Chinn and Isacks, 1983; Lange et al., 2009; Sielfeld et al.,
461 2019a; Pérez-Estay et al., 2020). This aligns with the global catalog results
462 shown earlier (Fig. 2). Conversely, the coexistence of reverse and strike-slip
463 focal mechanisms has been recorded only within the Main Cordillera between
464 33° and 34° S (e.g., Farías et al., 2006; Ammirati et al., 2019) (Fig. 4A). This
465 transition from radial shortening observed north of 34° S (non-partitioned) to
466 partitioned deformation south of 34° S, coincides with a marked increase in
467 convergence obliquity south of 34° S, related to a significant change in trench
468 orientation from nearly N-S to NNE.

469 (2) In the Maipo area (Fig. 4A), the P–T axes exhibit high dispersion, likely
470 related to local stress perturbations around faults, but reverse kinematics
471 predominate. The nodal plane covers a wide range of orientations, but nearly
472 N–S and E–W trending P-axis solutions are prevalent. Strike-slip kinematics
473 are consistent with predominant E–W shortening.

474 (3) Farther south, in the Araucanía and Aysén regions (Fig. 4B, C), margin-
475 parallel, strike-slip kinematics predominate, with NE-trending shortening
476 consistent with either dextral slip in subvertical N-to-NNE striking faults, or
477 sinistral slip in WNW-striking faults. Local observations of extensional

478 kinematics are detected, with nodal fault planes consistent with ENE-striking
479 normal faults.

480 (4) Strike-slip deformation in the arc domain, coherent with ~N–S striking mapped
481 dextral faults, suggests a northward motion of the forearc sliver, accompanied
482 by margin-parallel shortening at its leading edge, i.e., a buttress effect (Beck
483 et al., 1993; Lavenu and Cembrano, 1999; Fariás et al., 2006).

484 4. DISCUSSION

485 4.1. Exploring the role of margin-parallel versus transverse faults on slip 486 partitioning

487 Subtle but sharp along-strike variations in the continental margin trend affect the
488 magnitude of the strike-slip component derived from the oblique convergence vector.
489 (e.g., Stanton-Yonge et al., 2016; Fig. 2). In the end-member scenario of complete
490 slip partitioning (Fig. 1A), where slip at the plate interface exclusively accommodates
491 the margin-normal component of convergence, the total margin-parallel component
492 that should be accommodated by intra-arc faulting is estimated to be ~35 mm/year
493 between 33° and 38° S and ~24 mm/year between 38° and 47° S.

494 Under a complete partitioning scenario, the slip vectors of subduction earthquakes
495 would be oriented orthogonal to the margin (Beck, 1991; McCaffrey, 1992).
496 However, Stanton-Yonge et al. (2016) obtained an average slip direction of N89°E
497 by analyzing 20 subduction earthquakes for the 33-39° S region. This indicates that
498 slip at the plate interface accommodates only part of the oblique convergence,
499 suggesting partial partitioning in this segment (Fig. 1B). The difference between the
500 convergence vector and the thrust earthquake slip vectors leads to a residual slip
501 vector of 13.5 mm/year of margin-parallel displacement, which should be

502 accommodated in the upper plate between 33° and 38° S, and 12.1 mm/year
503 between 38° and 47° S (Fig. 2).

504 Applying the same analysis to a more recent subduction earthquake that occurred at
505 43° S (December 2016; Mw 7.6), the slip vector has a trend of N93°E, which is close
506 to the margin-orthogonal orientation (~N100°E). This indicates a more complete
507 partitioning toward the southern end of the study area and, consequently, a larger
508 margin-parallel slip component that must be accommodated within the upper plate
509 (~17 mm/year).

510 Fault slip estimates at the northern end of the LOFS, whether seismic or aseismic,
511 can reach as high as 18 mm/year (Astudillo-Sotomayor et al., 2021). However, this
512 finding poses a potential inconsistency: even if the single fault examined by
513 Astudillo-Sotomayor et al. (2021) accounted for all margin-parallel slip vectors, the
514 slip rate should be only ~13 mm/year, which is the expected end-member of partial
515 partitioning (Stanton-Yonge et al., 2016). Furthermore, because the LOFS consists
516 of multiple subparallel strands, the overall potential slip should be accommodated
517 across multiple faults. It is also important to note that *in situ* block rotation and
518 permanent distributed strain across the upper plate have been documented,
519 deformation components that also contribute to accommodating the oblique
520 convergence at the plate margin (García et al., 1988; Rojas et al., 1994; Cembrano
521 et al., 2002; Hernández et al., 2014, 2016). A plausible explanation for the unusually
522 high slip rate observed by Astudillo-Sotomayor et al. (2021) is that the northward
523 displacement of the forearc sliver, driven by the Chile Ridge subduction at 46° S,
524 may significantly amplify dextral strike-slip along margin-parallel faults (e.g., Forsythe
525 and Nelson, 1985; Cande and Leslie, 1986; Cembrano et al., 2002). On the other

526 hand, at the southernmost segment of the LOFS (~46° S), De Pascale et al. (2021)
527 suggested a Quaternary dextral slip rate of 11 to 24 mm/year based on displaced
528 glacial landforms, calculations that however should be interpreted with caution, as
529 the dates of the glacial landforms are not sufficiently well-constrained.

530 Regarding the role of margin-parallel versus margin-oblique faults in slip partitioning,
531 transverse faults can effectively accommodate part of the margin-orthogonal
532 component of oblique convergence across the submerged forearc, arc, and back-arc
533 regions (e.g., Sielfeld et al. 2019b). This observation supports the concept of
534 kinematic partitioning of overall transpressional deformation at all scales, from
535 regional to local (Fig. 1C). Transverse faults may also accommodate different long-
536 and short-term, along-strike shortening when acting as transfer faults (e.g.,
537 Arriagada et al. 2000), where faults can switch displacement sense at various time
538 scales.

539 **4.2. The seismic versus aseismic nature of long-term fault slip**

540 While there is a significant spatial correlation between long-term faulting and current
541 crustal earthquakes, the extent to which slip is accommodated through seismic and
542 aseismic processes remains elusive. This uncertainty has important implications for
543 our understanding of fault mechanics in the upper crust and for estimates of a fault's
544 seismic potential.

545 In the study area, mesoscopic fault surfaces with striae (slickensides) typically show
546 one or more of the following features: ridge-and-groove striae, mineral fibers, mineral
547 precipitation behind fault steps, breccia patches, and gouge (Fig. 5). The widespread
548 presence of mineral fibers behind fault steps rather than bladed calcite (believed to
549 be representative of seismic slip), along with the apparent lack of pseudotachylytes

550 (friction-induced melts), suggests that most of the mapped mesoscopic faults
551 represent aseismic slip.

552 The debate surrounding whether fault surfaces and their kinematic indicators, as
553 observed in the field, represent seismic slip or slow slip has persisted for decades
554 (Rowe and Griffith, 2015, and references therein). One interpretation of aseismic
555 creep involves mineral fibers and the pressure solution process. Pressure solution is
556 an effective mechanism that dissolves asperities that hinder fault slip and promotes
557 the growth of mineral fibers within fault slip zones (e.g., Gratier and Gamond, 1990;
558 Gratier et al., 2011). It includes successive stages: dissolution, transfer, and
559 deposition, indicating a slow displacement that is not relevant to the dynamic
560 movement of large earthquakes (e.g., Rutter, 1983). However, recent studies
561 suggest that creep processes may not relieve tectonic stress sufficiently to prevent
562 earthquake rupture, and some have even proposed that a creeping fault could still
563 produce large-magnitude earthquakes (e.g., Noda and Lapusta, 2013; Chen and
564 Bürgmann, 2017).

565 The lack of evidence for seismic slip in an exhumed fault zone does not exclude a
566 seismogenic history. For example, pseudotachylytes are among the most reliable
567 indicators of paleo-seismic slip (Rowe and Griffith, 2015). Experimental research
568 indicates that they can form after only millimeters of seismic slip (e.g., Niemeijer et
569 al., 2011), suggesting that they should be common in seismogenic faults.
570 Pseudotachylytes are, however, rarely reported in the literature, possibly due to the
571 difficulty in identifying them (e.g., Kirkpatrick and Rowe, 2013) and their rapid
572 removal from the geological record through hydrothermal alteration (e.g., Fondriest
573 et al., 2020). To our knowledge, with very local exceptions (see bladed calcite in

574 figure 5D), no conclusive seismic markers of any type have been documented along
575 the exhumed outcrops associated with the LOFS. This lack of field evidence,
576 however, does not preclude the LOFS from being seismogenic. In fact, the historic
577 seismicity linked to this fault (Fig. 2) provides clear evidence of its current
578 seismogenic nature, even though seismicity at the LOFS appears scattered and
579 relatively infrequent for a fault that likely accommodates long-term slip rates of up to
580 20 mm/yr. The apparent mismatch between the fault's activity and its estimated long-
581 term slip rates, combined with evidence in favor of paleo-aseismic slip, suggests that
582 part of the slip may occur without earthquakes (e.g., Astudillo et al. 2023). A
583 thorough characterization and quantification of the division between seismic and
584 aseismic slip along the LOFS is beyond the scope of this study and would require
585 detailed, long-term geodetic measurements.

586 **4.3. The role of hot fluids in intra-arc brittle deformation**

587 Records of crustal seismicity show more concentrated, intense activity in the intra-
588 arc domain than in the adjacent forearc and back-arc regions (e.g., Weller, 2012).
589 Additionally, whereas crustal seismicity in these latter two regions can reach depths
590 of ~30 km, the typical depth of the crustal seismogenic zone in the intra-arc is ~10
591 km. The inverse relationship between brittle crustal thickness and the geothermal
592 gradient supports the idea that active magmatic regions experience higher strain
593 rates, promoting feedback between fracturing, increased permeability, and fluid flow
594 (e.g., Rowland and Simmons, 2012). Rock strength decreases when fluids are
595 present within the rock-mass porosity, leading to greater damage under a given far-
596 field differential stress (Lockner, 1995). Conversely, the absence of fluids results in
597 less strain under the same stress regime. Therefore, the combined effect of a thin,

598 brittle volume containing fluid will cause concentrated damage and larger slip
599 magnitudes than those otherwise predicted from mechanical strain partitioning alone.
600 Although no quantitative studies have yet shown the exact amount of slip contributed
601 by these combined factors, we expect it to be on the order of a few millimeters per
602 year.

603 **4.4. Significance of long- and short-term kinematics in the along- and across-** 604 **strike segmentation of the Southern Andes**

605 Our new and revised compilation of fault slip data, along with crustal earthquake
606 focal mechanisms from global and local networks, provides an improved
607 understanding of the nature of slip partitioning between 33° and 47° S. Four main
608 segments are proposed (Fig. 6):

- 609 1. 33-34° S, characterized by a very small oblique convergence angle and no
610 margin-parallel intra-arc faulting. E-W shortening is accommodated by ENE
611 dextral and WNW sinistral strike-slip faults within the arc domain, and by
612 margin-parallel reverse faults in the back-arc (e.g., Ammirati et al., 2022).
613 Deformation in this segment is also characterized by several local Quaternary
614 faults in the forearc and arc regions, consistent with ~N–S shortening (Lavenu
615 and Cembrano, 2008, 2009). These faults are kinematically consistent with
616 present-day earthquake focal mechanisms (Figs. 2 and 4). The coexistence of
617 ~E–W and ~N–S shortening in this segment can be explained by a radial
618 compression strain/stress field, particularly along the WNW boundary zone
619 (here named the Maipo deformation zone) between segments 1 and 2. The
620 Maipo deformation zone occurs at the Maipo Orocline, and coincides with a
621 regional WNW magnetic anomaly and surface faults (Wall et al., 1996; Yáñez

622 et al., 1998, 2024; Arriagada et al., 2013; Piquer et al., 2021). Radial
623 compression at the southern boundary of this segment was suggested by
624 Allmendinger et al. (2006) based on independent GPS and geological data.
625 The Maipo boundary also marks a sharp transition in rock exhumation and an
626 elevation drop of about 2 km in the Main Cordillera (Figs. 2 and 6), also
627 coinciding with a key geological discontinuity where the Frontal Cordillera
628 ends (e.g., Ramos et al., 1986).

629 2. 34-37° S, characterized by a more pronounced oblique convergence,
630 partitioned into margin-parallel dextral faults and margin-oblique transverse
631 faults. The first ones are mostly blind, i.e., documented almost exclusively by
632 earthquake focal mechanisms, yet with a few exceptions (e.g., the El Melado
633 Fault; Cardona et al., 2018; Sielfeld et al., 2019b). At around 35.5° S, a set of
634 ENE-striking dextral transtensional faults is spatially associated with a marked
635 shift in the location of the present-day volcanic arc front (e.g., Sielfeld et al.,
636 2019b; Ruz-Ginouves et al., 2020). In this segment, a portion of the margin-
637 orthogonal shortening component is accommodated by WNW sinistral
638 transpressional faults and NE dextral faults, of which the former appears to be
639 seismically active (Stanton-Yonge et al., 2016, 2025; Vigide et al., 2025). The
640 boundary between segments 2 and 3 corresponds to a set of NW-striking
641 faults, of which the most prominent is the Lanalhue Fault (e.g., Melnick et al.,
642 2009). This boundary also coincides with significant latitudinal changes in
643 exhumation levels, especially in the forearc region. We propose that this
644 boundary is a crustal-scale, steeply dipping, south-verging reverse fault, in
645 accordance with the work by Melnick et al. (2009).

646 3. 37-41°S. This segment features a well-documented margin-parallel slip
647 component, accommodated by the LOFS and by seismically active NW and
648 NE strike-slip faults. The emerged forearc region is characterized by margin-
649 parallel shortening active since at least the late Pliocene epoch, as suggested
650 by fault slip data and current focal mechanisms. The ~N–S shortening is
651 probably a consequence of a buttress effect acting on the leading edge of the
652 northward-moving forearc sliver (e.g., Beck et al., 1993; Melnick et al., 2009;
653 Astudillo et al., 2023). The southern boundary of this segment is marked by
654 the WNW-striking Chacao Fault System north of Chiloé Island. Surface
655 geology reveals, in this southern end, a contrast in exhumation levels,
656 particularly along the volcanic arc, where mylonites to the north give way to
657 brittle faults to the south (e.g., Cembrano et al. 2000).

658 The LOFS ends as an extensional imbricate fan (horsetail structure) at around
659 38° S and connects with the Antñir-Copahue Fault System in the back-arc
660 (Folguera et al., 2004; Melnick et al., 2006; Pérez-Flores et al., 2016).

661 Regardless of how dextral strike-slip motion is accommodated at the northern
662 end of the LOFS, the northward movement of the forearc sliver should
663 decrease to nearly zero at the same latitude. This is because fault
664 displacement should be maximum at the central or trailing segments of any
665 strike-slip fault, naturally tapering off approaching their leading edge,
666 especially when they are buttressed (e.g., Beck et al. 1993). This creates a
667 latitudinal displacement gradient, resulting in margin-parallel shortening of the
668 forearc accompanied by counterclockwise tectonic rotation (e.g., Hernández-
669 Moreno, 2014, 2016). Margin-parallel shortening has also been observed in
670 the forearc of northern Chile (González et al., 2008; Allmendinger and

671 González, 2010), where conspicuous E–W faults are currently active. A
672 similar pattern of margin-parallel shortening and block rotation has been found
673 in the forearc of Cascadia (e.g., Johnson et al. 2004). In Cascadia, as well as
674 in the Southern Andes, roughly E–W margin-normal compression dominates
675 the forearc region near the trench, where the plates appear to be locked. In
676 contrast, when slow slip and tectonic tremors dominate the subduction
677 interface, and the plates are less strongly coupled, the forearc begins to
678 accommodate the margin-parallel shortening through strike-slip and thrust at
679 transverse crustal faults (e.g., Balfour et al., 2011).

680 4. 41-47° S. This segment accommodates most of the upper plate deformation
681 through a transtensional strike-slip duplex composed of two right-stepping
682 margin-parallel dextral strike-slip faults joined by NE-trending normal and
683 dextral-normal faults (Cembrano et al., 1996). Fault-slip data and earthquake
684 focal mechanisms are internally consistent with the long-term kinematics of
685 the LOFS (Arancibia et al., 1999; Lavenu and Cembrano, 1999; Cembrano et
686 al., 2002; Pérez-Estay et al., 2020). The northward, margin-parallel motion of
687 the forearc sliver is strongly supported by geological, geodetic,
688 paleomagnetic, and seismological data (Beck et al., 1993; Rojas et al., 1994;
689 Cembrano et al., 2000; Wang et al., 2007; Melnick et al., 2009; Moreno et al.,
690 2016; Sielfeld et al., 2019a).

691 Tectonic boundaries between segments 1-2 and 2-3 are interpreted in this work as
692 major, deep-seated south-verging reverse faults. The boundary between segments
693 3-4 is also a crustal-scale fault, although there is no clear evidence of vergence.
694 Based on geological mapping and geophysical evidence, Yáñez et al. (2024)
695 identified these features as first-order, long-lived tectonic structures, likely active

696 since at least the Permo-Triassic. During the Neogene-Quaternary, these faults have
697 influenced the location of volcanic alignments and ore deposits in the arc domain
698 (e.g., Lara et al., 2004; Cembrano and Lara, 2009; Piquer et al., 2015).

699 **4.5. Implications for seismic hazard**

700 Local paleo-seismological, geophysical, and morphological studies focused on
701 specific fault strands have provided estimates of their geometry, kinematics, and
702 recurrence intervals for the studied area. Notable examples include the works of
703 Vargas et al. (2014) and Yáñez et al. (2020) on the west-verging, reverse San
704 Ramon Fault in the Andean foothills of Santiago (33.5° S), with slip rates estimated
705 between 0.3-0.5 mm/year. At around 36° S, Vega-Ruiz et al. (2025) investigated
706 Quaternary deformation along the western margin of the Main Cordillera driven by
707 west-verging reverse faults, obtaining slip rates of up to 0.58 mm/year and estimated
708 a maximum M_w of 7.0. Further south, in the LOFS domain, morphotectonic analyses
709 of well-exposed master and splay faults have revealed slip rates of 10-22 mm/year
710 (Astudillo et al., 2018, 2021, 2023; De Pascale et al. 2021), significantly higher when
711 compared to estimates in the north. However, smaller slip-rate values are obtained
712 from numerical modeling: 1 to 7 mm/year for the margin-parallel LOFS, ~1 mm/year
713 for the Andean transverse faults, and 5-10 mm/year along the southern master faults
714 of the LOFS (e.g., Stanton-Yonge et al., 2016; Iturrieta et al., 2017).

715 While these studies have greatly enhanced our understanding of seismic hazards in
716 Chile, there has been a lack of systematic efforts to contextualize the fault systems
717 within a broader tectonic framework. Specifically, there has been insufficient
718 discussion of their role in plate margin partitioning and of the interplay between the
719 seismic and aseismic components of the reported fault displacements. Moreover,

720 long-term evidence of fault slip for many of these potentially hazardous faults has not
721 been critically integrated into the discussion surrounding the primary geological
722 processes involved, complicating comparisons with short-term deformation
723 observations. However, compilations focused on the nature and spatial distribution of
724 Quaternary crustal faults in the studied region (e.g., Lavenu et al., 2000; Santibañez
725 et al., 2019; Maldonado et al., 2021) are available, while Costa et al. (2020)
726 presented a compilation of Quaternary faults for South America and provided an
727 estimation of the regional-scale seismic hazard.

728 In terms of seismic hazard, our synthesis of crustal seismicity and long-term fault-slip
729 data suggests the following:

730 1. Aseismic slip should be considered when interpreting data from
731 morphotectonic analyses and fault separation of markers in potentially
732 seismogenic faults (e.g., LOFS). In fact, Astudillo et al. (2023) observed a
733 discrepancy between their estimated slip rates and the recurrence times of
734 historical earthquakes in the LOFS, with aseismic slip required to reconcile the
735 two. This observation is consistent with long-term evidence of displacement in
736 mesoscopic faults within the same fault systems where Holocene fault slip
737 estimates have been made, indicating that these faults exhibit a significant
738 amount of aseismic slip, as demonstrated by the presence of slickenfibers on
739 fault surfaces and shear bands, which are commonly used as kinematic
740 indicators (e.g., Pérez-Flores et al. 2016). Evidence for seismic slip in fossil faults
741 is often elusive (e.g., Rowe and Griffith, 2015), and only specific microstructures
742 indicate dynamic rupturing. The primary implication of the above points is that
743 many morphotectonic and paleo-seismological studies may significantly

744 overestimate seismic fault-slip rates, thereby exaggerating deterministic
745 estimates of earthquake magnitudes (e.g., Burgmann, 2018).

746 2. The tectonic transitions between the proposed segments identified in
747 this study are likely to play (and have played) a crucial role in the seismo-tectonic
748 segmentation of the margin. For instance, Yáñez et al. (2024) suggested that
749 trans-lithospheric faults have acted as regions of weak coupling, functioning as
750 long-term, geologically controlled seismic barriers. The release of fluids from the
751 Wadati-Benioff zone could be the driving force behind this creep-like mechanism.
752 Ample evidence of reverse faulting in these boundary zones is a key factor in
753 understanding these potential seismic barriers.

754 3. In probabilistic seismic hazard analysis (PSHA; e.g., Gerstenberger et
755 al., 2020), the contribution of crustal faults should be evaluated alongside the
756 dominant subduction interface hazard. In addition, because crustal sources are
757 typically shallow and near the sites of analysis, they can locally elevate seismic
758 hazard within a narrow spatial range. In the near-fault region, the long-return-
759 period tail of the hazard curve can be controlled by the fault itself, even when its
760 occurrence rates are low (e.g., Youngs and Coppersmith, 1985; Baker, 2013). In
761 our compiled instrumental catalog, the maximum documented magnitudes for
762 intra-arc events are Mw 6.5 in the north and Mw 6.2 in the south. Traditional
763 PSHA studies complement seismicity observations by constraining the maximum
764 magnitude and the magnitude-frequency distribution using mapped fault
765 geometries and slip rates (e.g., Gerstenberger et al., 2020). Despite notable
766 efforts to characterize faults in Chile (e.g., Santibáñez et al., 2019; Maldonado et
767 al., 2021), further work is needed to determine slip rates across all seismogenic
768 faults in a harmonized, systematic manner (e.g., Seebeck et al., 2023; Basili et

769 al., 2024). Future PSHA would certainly benefit from more accurate estimates on
770 interseismic slip rates from geodesic and remote sensing data (e.g., Chaussard
771 et al., 2016), along with physics-based rupture models, to explore the seismic
772 potential of crustal faults, including the contribution of slow slip to the earthquake
773 cycle (e.g., Bürgmann, 2018). For instance, dense, near-fault Global Navigation
774 Satellite System surveys could geodetically constrain interseismic strain, steady
775 creep, and/or transient slow-slip events (e.g., Rousset, 2019), thereby better
776 constraining the seismic slip deficit relevant for hazard assessment.

777 **5. CONCLUSIONS**

778 The combination of new and unpublished fault-slip data, and of regional and local
779 crustal seismicity, enables an updated understanding of the geometry and
780 kinematics of slip partitioning along and across the South American plate boundary
781 between 33° and 47° S. This partitioning proves to be much more complex than
782 previously thought, with implications for plate-margin tectonics, the spatial and
783 temporal distribution of fault slip, and interactions with other processes such as
784 active faulting and volcanism.

785 Slight variations in the along-strike orientation of the continental margin influence
786 different stress and strain distributions. Radial shortening (constriction) dominates
787 the Maipo Orocline region between 33° and 34° S, as margin-orthogonal and margin-
788 parallel shortening spatially coincide in a zone where there is a transition from non-
789 partitioned to partitioned deformation. Another important change occurs at around
790 37° S, where the strike-slip component of the convergence vector is reduced, and
791 the transcurrent margin-parallel slip is absorbed by a major, continuous intra-arc fault
792 system, the LOFS, between 37° and 46° S. Region-wide, the predominantly E–W

793 shortening documented in the submarine forearc contrasts with the margin-parallel
794 shortening observed from seismicity and fault slip data along the emerged forearc
795 region. In the arc domain, a combination of E–W shortening and NE–SW shortening,
796 the latter accommodated by a mostly hidden dextral fault between 34° and 37° S, is
797 then replaced to the south by a continuous surface expression of dextral faulting and
798 transverse, seismically active NE and NW dextral and sinistral faults.

799 The forearc sliver between 33° and 47° S is divided into four main blocks, separated
800 by prominent WNW- to NW-striking fault zones that may or may not extend into the
801 volcanic arc region. At the Maipo Orocline zone, a WNW transverse deformation
802 zone/fault places deeper crustal levels in the north over shallower levels in the south,
803 indicating a predominantly south-verging reverse fault or deformation zone. Surface
804 faults, such as Melipilla, Piuquencillo, and Pichilemu, are believed to be surface
805 expressions of this WNW deformation boundary. Farther south, at the Arauco
806 Peninsula region, where the continental margin shifts from a NNE to a ~N-S
807 orientation, another major NW-striking boundary separates Silurian-to-Permian
808 metamorphic rocks and intrusives to the north from mostly Paleozoic metamorphic
809 rocks to the south. As noted in previous works, this boundary is represented at the
810 surface by the NW-striking, south-verging Lanalhue reverse fault, which tends to
811 fade toward the volcanic arc. The fourth and last crustal block lies south of the
812 WNW-striking, mostly reverse, south-verging Chacao Fault, and is dominated by the
813 LOFS strike-slip duplex as the main tectonic element, which mostly accommodates
814 dextral strike-slip deformation.

815 Finally, in the LOFS, evidence for mostly slow slip (observed on exhumed striated
816 fault surfaces from where instantaneous shortening and extension axes were

817 derived) challenges the idea that these mesoscopic faults are fossil earthquake sites
818 and raises questions about whether seismic events are always the source of the
819 morphological and stratigraphic evidence of slip. It is therefore very likely that
820 calculated slip rates overestimate the seismic slip budget, thereby affecting seismic
821 hazard assessments.

822 **6. Acknowledgements**

823 The senior authors of this paper would like to warmly thank Francisco Hervé for
824 inspiring us in our early stages as independent researchers. This paper is dedicated
825 to him. Pancho introduced us to the Liquiñe-Ofqui Fault System in the late 1980s,
826 and from then on, it has captivated our interest and encouraged us to go further than
827 previous generations, along with many bright students, our junior coauthors, who are
828 now moving the frontiers of science. Numerous Fondecyt projects have generously
829 supported most of the research shown in this paper over the last few decades. The
830 first of these, headed by Pancho, was also supported by later projects shared with
831 Francisco Munizaga, Luis Lara, Hugo Moreno, Leopoldo López-Escobar, among
832 several others. The Andean Geothermal Center of Excellence, led by Diego Morata
833 and beginning in 2001, significantly advanced work in key areas of the Southern
834 Andes. We sincerely thank our friends Luis Lara and Gabriel González for the many
835 insightful discussions we have had over the years on the topics covered in this
836 paper. Many M.Sc. and Ph.D. ANID scholarships provided crucial funding for the
837 junior co-authors to develop innovative ideas on various topics related to slip
838 partitioning, using a combination of traditional geological and geophysical techniques
839 and cutting-edge numerical modeling.

840 Alain Lavenu's stay in Chile was funded by ORSTOM and later by IRD for several
841 years. This marked the start of research on the kinematic analysis of fault surfaces
842 and how this knowledge was passed down through generations in Chile.

843 Constanza Rojas and José Cembrano would like to thank Prof. Myrl Beck from
844 Western Washington University, who introduced them to the concept of slip
845 partitioning and paleomagnetism at convergent margins in the early 1990s. He is no
846 longer with us, but his passion for tectonic processes lives on in our hearts.

847 The manuscript was greatly improved thanks to the helpful comments from reviewers
848 Keith Klepeis and Carolina Canora. We are especially grateful to Guest Editor
849 Robert Pankhurst for his patient review, thoughtful editing, and careful handling of
850 the manuscript. Lastly, we sincerely thank Mauricio Calderón for encouraging us to
851 submit our work to this special issue.

852 **7. Data and Resources**

853 The GCMT (<https://www.globalcmt.org/>; Ekström et al., 2012) and ANSS-ComCat
854 (<https://earthquake.usgs.gov/>; U.S. Geological Survey, 2017) catalogs were last
855 accessed on August 1, 2025. Local-network hypocenters and focal mechanisms
856 were compiled from the published studies cited in the text. Slab geometry was
857 obtained from the Slab2 model (Hayes et al., 2018). Data processing and catalog
858 merging/classification were performed in Python, with the assistance of the obspy
859 (Beyreuther et al., 2010), pycsep (Savran et al., 2022), mplstereonet
860 (<https://pypi.org/project/mplstereonet/>), and FMC (Alvarez-Gomez, 2019) packages.
861 Fault-slip kinematic summaries and stereonet were generated with FaultKin
862 (Allmendinger et al., 2012). The final maps were prepared in QGIS
863 (<https://www.qgis.org>). All collected catalogs, fault kinematic measurements, and the

864 derived and processed datasets are archived in the accompanying Zenodo
865 repository: <https://doi.org/10.5281/zenodo.17296704>.

866

IN PRESS

867 **References**

- 868 Agurto, H.; Rietbrock, A.; Barrientos, S.; Bataille, K.; Legrand, D. 2012. Seismotectonic
869 structure of the Aysén Region, Southern Chile, inferred from the 2007 Mw=6.2 Aysén
870 earthquake sequence. *Geophysical Journal International* 190: 116-130.
871 <https://doi.org/10.1111/j.1365-246X.2012.05507.x>
- 872 Agurto-Detzel, H.; Rietbrock, A.; Bataille, K.; Miller, M.; Iwamori, H.; Priestley, K. 2014.
873 Seismicity distribution in the vicinity of the Chile Triple Junction, Aysén Region, southern
874 Chile. *Journal of South American Earth Sciences* 51: 1-11.
875 <https://doi.org/10.1016/j.jsames.2013.12.011>
- 876 Allmendinger, R.; Yáñez, G.; Cembrano, J. 2006. Instantaneous deformation associated with
877 flat subduction: Insights from GPS strain rates and numerical modelling. In *Congreso*
878 *Geológico Chileno*, No. 11, Actas 1: 367–370. Antofagasta, Chile.
- 879 Allmendinger, R.W.; González, G. 2010. Invited review paper: Neogene to Quaternary
880 tectonics of the coastal Cordillera, northern Chile. *Tectonophysics* 495 (1-2): 93-110.
881 <https://doi.org/10.1016/j.tecto.2009.04.019>
- 882 Allmendinger, R.W.; Cardozo, N.C.; Fisher, D. 2012. *Structural Geology Algorithms: Vectors*
883 *& Tensors*. Cambridge University Press. 289.
- 884 Álvarez-Gómez, J. A. 2019. FMC—Earthquake focal mechanisms data management, cluster
885 and classification. *SoftwareX*, 9, 299-307. <https://doi.org/10.1016/j.softx.2019.03.008>
- 886 Ammirati, J-B.; Vargas, G.; Rebolledo, S.; Abrahami, R.; Potin, B; Leyton, F.; Ruiz, S. 2019.
887 The crustal seismicity of the Western Andean Thrust (Central Chile, 33°-34°S):
888 implications for regional tectonics and seismic hazard in the Santiago area. *Bulletin of the*
889 *Seismological Society of America* 109 (5): 1985-1999.
890 <https://doi.org/10.1785/0120190082>
- 891 Ammirati, J-B.; Villaseñor, A.; Chevrot, S.; Easton, G.; Lehujeur, M.; Ruiz, S.; Flores, M.C.
892 2022. Automated earthquake detection and local travel time tomography in the South-
893 Central Andes (32-35°S): Implications for regional tectonics. *Journal of Geophysical*
894 *Research: Solid Earth* 127: e2022JB024097. <https://doi.org/10.1029/2022JB024097>
- 895 Angermann, D.; Klotz, J.; Reigber, C. 1999. Space-geodetic estimation of the Nazca-South
896 America Euler vector. *Earth and Planetary Sciences* 171 (3): 329-334.
897 [https://doi.org/10.1016/S0012-821X\(99\)00173-9](https://doi.org/10.1016/S0012-821X(99)00173-9)
- 898 Arancibia, G.; Cembrano, J.; Lavenu, A. 1999. Transpresión dextral y partición de la
899 deformación en la Zona de Falla Liquiñe-Ofqui, Aisén, Chile (44-45°S). *Revista Geológica*
900 *de Chile* 26 (1): 3-22. <http://dx.doi.org/10.4067/S0716-02081999000100001>
- 901 Aron, F.; Allmendinger, R.W.; Cembrano, J.; González, G.; Yáñez, G. 2013. Permanent fore-
902 arc extension and seismic segmentation: Insights from the 2010 Maule earthquake, Chile.
903 *Journal of Geophysical Research: Solid Earth* 118: 724-739.
904 <https://doi.org/10.1029/2012JB009339>

- 905 Arriagada, C.; Roperch, P.; Mpodozis, C. 2000. Clockwise block rotations along the eastern
906 border of the Cordillera de Domeyko, Northern Chile (22°45'-23°30' S). *Tectonophysics*
907 326 (1-2): 153-171. [https://doi.org/10.1016/S0040-1951\(00\)00151-7](https://doi.org/10.1016/S0040-1951(00)00151-7)
- 908 Arriagada, C., Ferrando, R., Córdova, L., Morata, D., & Roperch, P. (2013). The Maipo
909 Orocline: A first scale structural feature in the Miocene to Recent geodynamic evolution in
910 the central Chilean Andes. *Andean geology*, 40(3), 419-437.
911 <http://dx.doi.org/10.5027/andgeoV40n3-a02>
- 912 Astudillo, L.; Cortés-Aranda, J.; Melnick, D.; Tassara, A. 2018. Holocene deformation along
913 the Liquiñe–Ofqui Fault Zone, southern Chile: Field observations and geomorphic
914 analysis. In *International INQUA Meeting on Paleoseismology, Active Tectonics and*
915 *Archeoseismology (PATA)*, No. 9. Possidi, Greece.
- 916 Astudillo-Sotomayor, L.; Jara-Muñoz, J.; Melnick, D.; Cortés-Aranda, J.; Tassara, A.;
917 Strecker, M.R. 2021. Fast Holocene slip and localized strain along the Liquiñe–Ofqui
918 strike-slip fault system, Chile. *Scientific Reports* 11. [https://doi.org/10.1038/s41598-021-](https://doi.org/10.1038/s41598-021-85036-5)
919 [85036-5](https://doi.org/10.1038/s41598-021-85036-5)
- 920 Astudillo-Sotomayor, L.; Cortés-Aranda, J.; Melnick, D.; Jara-Muñoz, J.; Cabello, C.;
921 Perucca, L.; Tassara, A.; Pérez-Peña, J. V.; León-Ibáñez, P. 2023. Neotectonic faults in
922 the Southern Chile intra-arc (38°S-40.5°S): Insights about their seismic potential and the
923 link with the megathrust earthquake cycle. *Tectonophysics* 846, 229675.
924 <https://doi.org/10.1016/j.tecto.2022.229675>
- 925 Baker, J. W. 2013. Probabilistic seismic hazard analysis. White Paper Version 2.0.1: 79.
- 926 Balfour, N.J.; Cassidy, J.F.; Dosso, S.E.; Mazzotti, S. 2011. Mapping crustal stress and
927 strain in southwest British Columbia. *Journal of Geophysical Research: Solid Earth* 116
928 (B3): 1-11. <https://doi.org/10.1029/2010JB008003>
- 929 Barrientos, S.E.; Acevedo-Aránquiz, P.S.; 1992. Seismological aspects of the 1988-1989
930 Lonquimay (Chile) volcanic eruption. *Journal of Volcanology and Geothermal Research*
931 53: 73-87. [https://doi.org/10.1016/0377-0273\(92\)90075-o](https://doi.org/10.1016/0377-0273(92)90075-o)
- 932 Basili, R.; Danciu, L.; Beauval, C.; Sesetyan, K.; Pires Vilanova, S.; Adamia, S.; Arroucau,
933 P.; Atanackov, J.; Baize, S.; Canora, C.; Caputo, R.; Cosimo Carafa, M.M.; Cushing,
934 E.M.; Custódio, S.; Demircioglu Tumsa, M.B.; Duarte, J.C.; Ganas, A.; García-
935 Mayordomo, J.; Gómez de la Peña, J.; Gràcia, E.; Jamsek Rupnik, P.; Jomard, H.;
936 Kastelic, V.; Maesano, F.E.; Martín-Banda, R.; Martínez-Loriente, S.; Neres, M.; Perea,
937 H.; Sket Motnikar, B.; Tiberti, M.M.; Tsereteli, N.; Tsironi, V.; Vallone, R.; Vanneste, K.;
938 Zupancic, P.; Giardini, D. 2024. The European fault-source model 2020 (EFSM20):
939 Geologic input data for the European Seismic Hazard Model 2020. *Natural Hazards and*
940 *Earth System Sciences* 24 (11): 3945-3976. <https://doi.org/10.5194/nhess-24-3945-2024>
- 941 Beck Jr., M.E. 1991. Coastwise transport considered: Lateral displacements in oblique
942 subduction zones, and tectonic consequences. *Physics of the Earth and Planetary*
943 *Interiors* 68: 1-8.

- 944 Beck Jr., M.E.; Rojas, C.; Cembrano, J. 1993. On the nature of buttressing in margin-parallel
945 strike-slip fault systems. *Geology* 21 (8): 755-758.
- 946 Beyreuther, M.; Barsch, R.; Krischer, L.; Megies, T.; Behr, Y.; Wassermann, J. 2010.
947 ObsPy: A Python toolbox for seismology. *Seismological Research Letters*, 81(3): 530-
948 533. <https://doi.org/10.1785/gssrl.81.3.530>
- 949 Bravo, F.; Koch, P.; Riquelme, S.; Fuentes, M.; Campos, J. 2019. Slip distribution of the
950 1985 Valparaíso earthquake constrained with seismic and deformation data.
951 *Seismological Research Letters*, 90 (5): 1792-1800. <https://doi.org/10.1785/0220180396>
- 952 Bürgmann, R. 2018. The geophysics, geology and mechanics of slow fault slip. *Earth and*
953 *Planetary Science Letters* 495 (1): 112-134. <https://doi.org/10.1016/j.epsl.2018.04.062>
- 954 Cande, S.C.; Leslie, R.B. 1986. Late Cenozoic tectonics of the Southern Chile Trench.
955 *Journal of Geophysical Research: Solid Earth* 91 (B1): 471-496.
956 <https://doi.org/10.1029/JB091iB01p00471>
- 957 Canora, C.; Martínez-Díaz, J.; Villamor, P.; Staller, A.; Berryman, K.; Álvarez-Gómez, J.A.;
958 Capote, R.; Diaz, M. 2014. Structural evolution of the El Salvador Fault Zone: An evolving
959 fault system within a volcanic arc. *Journal of Iberian Geology* 40 (3): 471-488.
960 https://doi.org/10.5209/rev_JIGE.2014.v40.n3.43559
- 961 Cardona, C.; Tassara, A.; Gil-Cruz, F.; Lara, L.; Morales, S.; Kohler, P.; Franco, L. 2018.
962 Crustal seismicity associated to rapid surface uplift at Laguna del Maule Volcanic
963 Complex, Southern Volcanic Zone of the Andes. *Journal of Volcanology and Geothermal*
964 *Research* 353: 83-94. <https://doi.org/10.1016/j.jvolgeores.2018.01.009>
- 965 Cembrano, J.; Hervé, F.; Lavenu, A. 1996. The Liquiñe Ofqui fault zone: a long-lived intra-
966 arc fault system in southern Chile. *Tectonophysics* 259 (1-3): 55-66.
967 [https://doi.org/10.1016/0040-1951\(95\)00066-6](https://doi.org/10.1016/0040-1951(95)00066-6)
- 968 Cembrano J.; Schermer, E.; Lavenu, A.; Sanhueza, A. 2000. Contrasting nature of
969 deformation along an intra-arc shear zone, the Liquiñe-Ofqui fault zone, southern Chilean
970 Andes. *Tectonophysics* 319 (2): 129-149. [https://doi.org/10.1016/S0040-1951\(99\)00321-2](https://doi.org/10.1016/S0040-1951(99)00321-2)
- 971 Cembrano, J.; Lavenu, A.; Reynolds, P.; Arancibia, G.; López, G.; Sanhueza, A. 2002. Late
972 Cenozoic transpressional ductile deformation north of the Nazca-South America-
973 Antarctica triple junction. *Tectonophysics* 354 (3-4): 289-314.
974 [https://doi.org/10.1016/S0040-1951\(02\)00388-8](https://doi.org/10.1016/S0040-1951(02)00388-8)
- 975 Cembrano, J.; Lara, L. 2009. The link between volcanism and tectonics in the southern
976 volcanic zone of the Chilean Andes: A review. *Tectonophysics* 471: 96-113.
977 <https://doi.org/10.1016/j.tecto.2009.02.038>
- 978 Charrier, R.; Baeza, O.; Elgueta, S.; Flynn, J.J.; Gans, P.; Mahlburg Kay, S. ; Muñoz, N. ;
979 Wyss, A.R. ; Zurita, E. 2002. Evidence for Cenozoic extensional basin development and
980 tectonic inversion south of the flat-slab segment, southern Central Andes, Chile (33°S-
981 36°S.L.). *Journal of South American Earth Sciences* 15 (1): 117-139.
982 [https://doi.org/10.1016/S0895-9811\(02\)00009-3](https://doi.org/10.1016/S0895-9811(02)00009-3)

- 983 Chaussard, E.; Bürgmann, R.; Fattahi, H.; Johnson, C.W.; Nadeau, R.M. 2016. Potential and
984 limits of InSAR to characterize interseismic deformation independently of GPS data:
985 Application to the southern San Andreas Fault system. *Geochemistry, Geophysics,
986 Geosystems* 17 (3): 1214-1229. <https://doi.org/10.1002/2015GC006246>
- 987 Chen, K.H.; Bürgmann, R. 2017. Creeping faults: good news, bad news? *Reviews of
988 Geophysics* 55 (2): 282-286. <https://doi.org/10.1002/2017RG000565>
- 989 Chinn, D.S.; Isacks, B.I. 1983. Accurate source depths and focal mechanisms of shallow
990 earthquakes in western South America and in the New Hebrides Island arc. *Tectonics* 2:
991 529-563.
- 992 Costa, C.; Alvarado, A.; Audemard, F.; Audin, L.; Benavente, C.; Hilario Bezerra, F.;
993 Cembrano, J.; González, G.; López, M.; Minaya, E.; Santibañez, I.; Garcia J.; Acrila, M.;
994 Pagani, M.; Pérez, I.; Delgado, F.; Paolini, M.; Garro, H. 2020. Hazardous faults of South
995 America; compilation and overview. *Journal of South American Earth Sciences* 104.
996 <https://doi.org/10.1016/j.jsames.2020.102837>
- 997 De Pascale, G.; Froude, M.; Penna, I.; Hermanns, R.L.; Sepúlveda, S.A.; Moncada, D.;
998 Persico, M.; Easton, G.; Villalobos, A. A.; Gutierrez, F. 2021. Liquiñe-Ofqui's fast slipping
999 intra-volcanic arc crustal faulting above the subducted Chile Ridge. *Scientific Reports* 11.
1000 <https://doi.org/10.1038/s41598-021-03919-z>
- 1001 de Saint Blanquat, M.; Tikoff, B.; Teyssier, C.; Vigneresse, J.L. 1998. Transpressional
1002 kinematics and magmatic arcs. *Geological Society, London, Special Publications* 135:
1003 327-340. <https://doi.org/10.1144/GSL.SP.1998.135.01.21>
- 1004 Eisermann, J.O.; Göllner, P.L.; Riller, U. 2021. Orogen-scale transpression accounts for
1005 GPS velocities and kinematic partitioning in the Southern Andes. *Communications Earth
1006 & Environment* 2 167. <https://doi.org/10.1038/s43247-021-00241-4>
- 1007 Ekström, G.; Nettles, M.; Dziewoński, A.M. 2012. The global CMT project 2004–2010:
1008 Centroid-moment tensors for 13,017 earthquakes. *Physics of the Earth and Planetary
1009 Interiors* 200: 1-9. <https://doi.org/10.1016/j.pepi.2012.04.002>
- 1010 Farías, M.; Comte, D.; Charrier, R. 2006. Sismicidad superficial en Chile central:
1011 Implicancias para el estado cortical y crecimiento de los Andes Centrales australes. In
1012 *Congreso Geológico Chileno, No. 11, Actas* 1: 403–406. Antofagasta, Chile.
- 1013 Farías, M.; Charrier, R.; Carretier, S.; Martinod, J.; Fock, A.; Campbell, D.; Cáceres, J.;
1014 Comte, D. 2007. Late Miocene high and rapid surface uplift and its erosional response in
1015 the Andes of central Chile (33°S-35°S). *Tectonics* 27 (1): 1-22.
1016 <https://doi.org/10.1029/2006TC002046>
- 1017 Farías, M.; Comte, D.; Roecker, S.; Carrizo, D.; Pardo, M. 2011. Crustal extensional faulting
1018 triggered by the 2010 Chilean earthquake: The Pichilemu Seismic Sequence. *Tectonics*
1019 30 (6): 1-11. <https://doi.org/10.1029/2011TC002888>

- 1020 Fitch, T.J. 1972. Plate convergence, transcurrent fault, and internal deformation adjacent to
 1021 Southeast Asia and the Western Pacific. *Journal of Geophysical Research* 77 (23): 4432-
 1022 4460.
- 1023 Folguera, A.; Ramos, V.A.; Melnick, D. 2002. Partición de la deformación en la zona del arco
 1024 volcánico de los Andes neuquinos (36-39°S) en los últimos 30 millones de años. *Revista*
 1025 *Geológica de Chile* 29 (2): 151-165. [http://dx.doi.org/10.4067/S0716-
 1026 02082002000200005](http://dx.doi.org/10.4067/S0716-02082002000200005)
- 1027 Folguera, A.; Ramos, V.A.; Hermanns, R.L.; Naranjo, J. 2004. Neotectonics in the foothills of
 1028 the southernmost central Andes (37°-38°S): evidence of strike-slip displacement along the
 1029 Antifñir-Copahue fault zone. *Tectonics* 23 (5): 1-23.
 1030 <https://doi.org/10.1029/2003TC001533>
- 1031 Folguera, A.; Introcaso, A.; Gimenez, M.E.; Ruiz, F.; Martinez, M.P.; Tunstall, C.; Garcia
 1032 Morabito, E.; Ramos, V.A. 2007. Crustal attenuation in the Southern Andean retroarc
 1033 (38°-39°30'S) determined from tectonic and gravimetric studies: The Lonco-Luán
 1034 asthenospheric anomaly. *Tectonophysics* 439(1); 129-147.
 1035 <https://doi.org/10.1016/j.tecto.2007.04.001>
- 1036 Fondriest, M.; Mecklenburgh, J.; Passelegue, F.X.; Artioli, G.; Nestola, F.; Spagnuolo, E.;
 1037 Rempe, M.; Di Toro, G., 2020. Pseudotachylyte alteration and the rapid fade of
 1038 earthquake scars from the geological record. *Geophysical Research Letters* 47 (22): 1-9.
 1039 <https://doi.org/10.1029/2020GL090020>
- 1040 Forsythe, R.; Nelson, E. 1985. Geological manifestations of ridge collision: Evidence from
 1041 the Golfo de Penas-Taitao Basin, Southern Chile. *Tectonics* 4 (5): 477-495.
 1042 <https://doi.org/10.1029/TC004i005p00477>
- 1043 Galland, O.; Hallot, E.; Cobbold, P.R.; Ruffet, G.; d'Ars, J.d.B. 2007. Volcanism in a
 1044 compressional Andean setting; a structural and geochronological study of Tromen
 1045 volcano (Neuquén province, Argentina). *Tectonics* 26 (4): 1-24.
 1046 <https://doi.org/10.1029/2006TC002011>
- 1047 García, A.R.; Beck, M.E.; Burmester, R.F.; Munizaga, F.E.; Hervé, F. 1988. Paleomagnetic
 1048 reconnaissance of the Region de Los Lagos, Southern Chile, and its tectonic implications:
 1049 *Revista Geológica de Chile* 15 (1): 13- 30.
- 1050 Gerbault, M.; Cembrano, J.; Mpodozis, C.; Farías, M.; Pardo, M. 2009. Continental margin
 1051 deformation along the Andean subduction zone: Thermo-mechanical models. *Physics of*
 1052 *the Earth and Planetary Interiors* 177: 180-205. <https://doi.org/10.1016/j.pepi.2009.09.001>
- 1053 Gerstenberger, M.C.; Marzocchi, W.; Allen, T.; Pagani, M.; Adams, J.; Danciu, L.; Field,
 1054 E.H.; Fujiwara, H.; Luco, N.; Ma, K.-F.; Meletti, C.; Petersen, M.D. 2020. Probabilistic
 1055 seismic hazard analysis at regional and national scales: State of the art and future
 1056 challenges. *Reviews of Geophysics* 58 (2): e2019RG000653.
 1057 <https://doi.org/10.1029/2019RG000653>

- 1058 Gerstenberger, M. C.; Bora, S.; Bradley, B. A.; DiCaprio, C.; Kaiser, A.; Manea, E.F.; Nicol,
1059 A.; Rollins, C.; Stirling, M.W.; Thingbaijam, K.K.S.; Van Dissen, R.J.; Abbott, E.R.;
1060 Atkinson, G.M.; Chamberlain, C.; Christophersen, A.; Clark, K.; Coffey, G.L.; de la Torre,
1061 C.A.; Ellis, S.M.; Fraser, J.; Graham, K.; Griffin, J.; Hamling, I.J.; Hill, M.P.; Howell, A.;
1062 Hulse, A.; Hutchinson, J.; Iturrieta, P.; Johnson, K.M.; Oakley Jurgens, V.; Kirkman, R.;
1063 Langridge, R.M.; Lee, R.L.; Litchfield, N.L.; Maurer, J.; Milner, K.R.; Rastin, S.;
1064 Rattenbury, M.S.; Rhoades, D.A.; Ristau, J.; Schorlemmer, D.; Seebeck, H.; Shaw, B.E.;
1065 Stafford, P.J.; Stolte, A.C.; Townend, J.; Villamor, P.; Wallace, L.M.; Weatherill, G.;
1066 Williams, C.A.; Wotherspoon, L.M. 2024. The 2022 Aotearoa New Zealand national
1067 seismic hazard model: Process, overview, and results. *Bulletin of the Seismological*
1068 *Society of America*, 114(1): 7-36. <https://doi.org/10.1785/0120230182>
- 1069 Giambiagi, L.B.; Ramos, V.A. 2002. Structural evolution of the Andes in a transitional zone
1070 between flat and normal subduction (33°30'-33°45'S), Argentina and Chile. *Journal of*
1071 *South American Earth Sciences* 15 (1): 101-116. [https://doi.org/10.1016/S0895-9811\(02\)00008-1](https://doi.org/10.1016/S0895-9811(02)00008-1)
- 1073 Giambiagi, L.; Mescua, J.; Bechis, F.; Tassara, A.; Hoke, G. 2012. Thrust belts of the
1074 southern Central Andes: Along-strike variations in shortening, topography, crustal
1075 geometry, and denudation. *GSA Bulletin* 124 (7-8): 1339-1351.
1076 <https://doi.org/10.1130/B30609.1>
- 1077 Glodny, J.; Echtler, H.; Collao, S.; Ardiles, M.; Burón, P.; Figueroa, O. 2008. Differential Late
1078 Paleozoic active margin evolution in South-Central Chile (37°S-40°S) -The Lanahue Fault
1079 Zone. *Journal of South American Earth Sciences* 26 (4): 397-411.
1080 <https://doi.org/10.1016/j.jsames.2008.06.001>
- 1081 González, G.; Allmendinger, R.; Dunai, T.; Cembrano, J.; Martinod, J.; Rémy, D.; Carrizo,
1082 D.; Loveless, J.P.; Veloso, E.E.; Aron, F.; Cortés-Aranda, J. 2008. The active upper plate
1083 deformation of the Central Andes forearc, northern Chile: the geological view. In
1084 *International Symposium on Andean Geodynamics (ISAG), No. 7, Extended Abstracts:*
1085 116-119. Nice, France.
- 1086 Gratier, J.P.; Gamond, J.F. 1990. Transition between seismic and aseismic deformation in
1087 the upper crust. *Geological Society, London, Special Publications* 54: 461-473.
1088 <https://doi.org/10.1144/GSL.SP.1990.054.01.42>
- 1089 Gratier, J.P.; Richard, J.; Renard, F.; Mittempergher, S.; Doan, M.L.; Di Toro, G.; Hadizadeh,
1090 J.; Boullier, A.M. 2011. Aseismic sliding of active faults by pressure solution creep:
1091 Evidence from the San Andreas Fault Observatory at depth. *Geology* 39 (12): 1131-1134.
1092 <https://doi.org/10.1130/G32073.1>
- 1093 Hayes, G. P.; Moore, G. L.; Portner, D. E.; Hearne, M.; Flamme, H.; Furtney, M.; Smoczyk,
1094 G.M. 2018. Slab2, a comprehensive subduction zone geometry model. *Science* 362
1095 (6410): 58-61. <https://doi.org/10.1126/science.aat4723>
- 1096 Hernández-Moreno, C.; Speranza, F.; Di Chiara, A. 2014. Understanding kinematics of intra-
1097 arc transcurrent deformation: Paleomagnetic evidence from the Liquiñe-Ofqui fault zone
1098 (Chile, 38-41°S). *Tectonics* 33 (10): 1964-1988. <https://doi.org/10.1002/2014TC003622>

- 1099 Hernandez-Moreno, C., F. Speranza, and A. Di Chiara 2016. Paleomagnetic rotation pattern
1100 of the southern Chile fore-arc sliver (38° S–42° S): A new tool to evaluate plate locking
1101 along subduction zones, *J. Geophys. Res. Solid Earth*, 121, 469–490,
1102 doi:10.1002/2015JB012382.
- 1103 Hervé, M., 1976. Estudio geológico de la falla Liquiñe-Reloncaví en el área de Liquiñe-
1104 Reloncaví, antecedentes de un movimiento transcurrente (Provincia de Valdivia). I Congr.
1105 Geol. Chil. Actas, I: B39-B56.
- 1106 Hervé, F., Araya, E., Fuenzalida, J.L. and Solano, A., 1979. Edades radiométricas y
1107 tectónica neógena en el sector costero de Chiloé Continental, X Región. II Congr. Geol.
1108 Chil. Actas, 1: FI-F8.
- 1109 Hervé, F. 1994. The Southern Andes between 39° and 44° S Latitude: The Geological
1110 Signature of a Transpressive Tectonic Regime Related to a Magmatic Arc. In: Reutter,
1111 K.J., Scheuber, E. and Wigger, P.J., Eds., *Tectonics of the Southern Central Andes*,
1112 Springer Verlag, Berlin, 243-248. https://doi.org/10.1007/978-3-642-77353-2_1
- 1113 Hervé, F.; Pankhurst, R.J.; Drake, R.; Beck, M.E. 1995. Pillow metabasalts in a mid-Tertiary
1114 extensional basin adjacent to the Liquiñe-Ofqui fault zone: the Isla Magdalena area,
1115 Aysén, Chile. *Journal of South American Earth Sciences* 8 (1): 33-46.
1116 [https://doi.org/10.1016/0895-9811\(94\)00039-5](https://doi.org/10.1016/0895-9811(94)00039-5)
- 1117 Iturrieta, P.C.; Hurtado, D.E.; Cembrano, J.; Stanton-Yonge, A. 2017. States of stress and
1118 slip partitioning in a continental-scale strike-slip duplex: Tectonic and magmatic
1119 implications by means of finite element modeling. *Earth and Planetary Science Letters*
1120 473 (1): 71-82. <https://doi.org/10.1016/j.epsl.2017.05.041>
- 1121 Jarrard, R.D. 1986. Relations among subduction parameters. *Reviews of Geophysics* 24 (2):
1122 217-284. <https://doi.org/10.1029/RG024i002p00217>
- 1123 Johnson, S.Y.; Blakely, R.J.; Stephenson, W.J.; Dadisman, S.V.; Fisher, M.A. 2004. Active
1124 shortening of the Cascadia forearc and implications for seismic hazards of the Puget
1125 Lowland. *Tectonics* 23 (1): 1-27. <https://doi.org/10.1029/2003TC001507>
- 1126 Jordan, T.E.; Isacks, B.L.; Allmendinger, R.W.; Brewer, J.A.; Ramos, V.A.; Ando, C.J. 1983.
1127 Andean tectonics related to geometry of subducted Nazca plate. *GSA Bulletin* 94: 341-
1128 361.: 297-306. [https://doi.org/10.1130/0016-
1129 7606\(1983\)94%3C341:ATRTGO%3E2.0.CO;2](https://doi.org/10.1130/0016-7606(1983)94%3C341:ATRTGO%3E2.0.CO;2)
- 1130 Kirkpatrick, J.D.; Rowe, C.D. 2013. Disappearing ink: How pseudotachylytes are lost from
1131 the rock record. *Journal of Structural Geology* 52: 183-198.
1132 <https://doi.org/10.1016/j.jsq.2013.03.003>
- 1133 Lange, D.; Cembrano, J.; Rietbrock, A.; Haberland, C.; Dahm, T.; Bataille, K. 2008. First
1134 seismic record for intra-arc strike-slip tectonics along the Liquiñe-Ofqui fault zone at the
1135 obliquely convergent plate margin of the southern Andes. *Tectonophysics* 445 (1-4): 14-
1136 24. <https://doi.org/10.1016/j.tecto.2008.04.014>

- 1137 Lara, L.E.; Naranjo, J.A.; Moreno, H. 2004. Rhyodacitic fissure eruption in the Southern
1138 Andes (Cordón Caulle; 40.5° S) after the 1960 (Mw 9.5) Chilean earthquake: A structural
1139 interpretation. *Journal of Volcanology and Geothermal Research* 138 (1–2): 127–138.
1140 <https://doi.org/10.1016/j.jvolgeores.2004.06.009>
- 1141 Lara, L.; Lavenu, A.; Cembrano, J.; Rodríguez, C. 2006. Structural controls of volcanism in
1142 transversal chains: Resheared faults and neotectonics in the Cordón Caulle-Puyehue
1143 area (40.5°S), Southern Andes. *Journal of Volcanology and Geothermal Research* 158 (1-
1144 2): 70-86. <https://doi.org/10.1016/j.jvolgeores.2006.04.017>
- 1145 Lavenu, A.; Cembrano, J. 1999. Compressional- and transpressional-stress pattern for
1146 Pliocene and Quaternary brittle deformation in fore arc and intra-arc zones (Andes of
1147 Central and Southern Chile). *Journal of Structural Geology* 21: 1669-1691.
1148 [https://doi.org/10.1016/S0191-8141\(99\)00111-X](https://doi.org/10.1016/S0191-8141(99)00111-X)
- 1149 Lavenu, A.; Thiele, R.; Machette, M.; Dart, R.; Bradley, L.-A.; Haller, K.M. 2000. Maps and
1150 database of Quaternary faults in Bolivia and Chile. U.S. Geological Survey, Open-File
1151 Report 00-283: 46 p.
- 1152 Lavenu, A.; Cembrano, J. 2008. Quaternary compressional deformation in the Main
1153 Cordillera of Central Chile (Cajón del Maipo, east of Santiago). *Revista Geológica de*
1154 *Chile* 35 (2): 233-252. <http://dx.doi.org/10.5027/andgeoV35n2-a03>
- 1155 Legrand, D.; Barrientos, S.; Bataille, K.; Cembrano, J.; Pavez, A. 2011. The fluid-driven
1156 tectonic swarm of Aysen Fjord, Chile (2007) associated with two earthquakes (Mw=6.1
1157 and Mw=6.2) within the Liquiñe-Ofqui Fault Zone. *Continental Shelf Research* 31 (3-4):
1158 154-161. <https://doi.org/10.1016/j.csr.2010.05.008>
- 1159 Lockner, D.A. 1995. Rock failure. *Rock physics and phase relations: A handbook of physical*
1160 *constants* (3):127-147.
- 1161 Maldonado, V.; Contreras, M.; Melnick, D. 2021. A comprehensive database of active and
1162 potentially-active continental faults in Chile at 1:25,000 scale. *Scientific Data* 8 (20).
1163 <https://doi.org/10.1038/s41597-021-00802-4>
- 1164 Marrett, R.; Allmendinger, R.W. 1990. Kinematic analysis of fault-slip data. *Journal of*
1165 *Structural Geology* 12 (8): 973-986. [https://doi.org/10.1016/0191-8141\(90\)90093-E](https://doi.org/10.1016/0191-8141(90)90093-E)
- 1166 McCaffrey, R. 1992. Oblique plate convergence, slip vectors, and forearc deformation.
1167 *Journal of Geophysical Research Atmospheres* 97 (B6): 8905-8915.
1168 <https://doi.org/10.1029/92JB00483>
- 1169 McCaffrey, R. 1996. Slip partitioning at convergent plate boundaries of SE Asia. *Geological*
1170 *Society, London, Special Publications* 106: 3-18.
1171 <https://doi.org/10.1144/GSL.SP.1996.106.01.02>
- 1172 Melnick, D.; Charlet, F.; Echtler, H.P., De Batist, M. 2006. Incipient axial collapse of the Main
1173 Cordillera and strain partitioning gradient between the central and Patagonian Andes,
1174 Lago Laja, Chile. *Tectonics* 25 (5): 1-22. <https://doi.org/10.1029/2005TC001918>

- 1175 Melnick, D.; Bookhagen, B.; Strecker, M.R.; Echtler, H.P. 2009. Segmentation of megathrust
1176 rupture zones from fore-arc deformation patterns over hundreds to millions of years,
1177 Arauco peninsula, Chile. *Journal of Geophysical Research* 114 (B1): B01407.
1178 <https://doi.org/10.1029/2008JB005788>
- 1179 Mescua, J.F.; Barrionuevo, M.; Giambiagi, L.; Suriano, J.; Spagnotto, S.; Stahlschmidt, E.;
1180 de la Cal, H.; Soto, J.L.; Mazzitelli, M.A. 2019. Stress field and active faults in the
1181 orogenic front of the Andes in the Malargüe fold-and-thrust belt (35°-36°S).
1182 *Tectonophysics* 766: 179-193. <https://doi.org/10.1016/j.tecto.2019.06.003>
- 1183 Montenegro, V.M.; Spagnotto, S.; Legrand, D.; Caselli, A.T. 2021. Seismic evidence of the
1184 active regional tectonic faults and the Copahue volcano, at Caviahue Caldera, Argentina.
1185 *Bulletin of Volcanology* 83 (20). <https://doi.org/10.1007/s00445-021-01442-7>
- 1186 Mora, C.; Comte, D.; Russo, R.; Gallego, A.; Mocanu, V. 2010. Aysén seismic swarm
1187 (January 2007) in southern Chile: analysis using Joint Hypocenter Determination. *Journal*
1188 *of Seismology* 14: 683-691. <https://doi.org/10.1007/s10950-010-9190-y>
- 1189 Moreno, M.S.; Bolte, J.; Klotz, J.; Melnick, D. 2009. Impact of megathrust geometry on
1190 inversion of coseismic slip from geodetic data: Application to the 1960 Chile earthquake.
1191 *Geophysical Research Letters* 36 (16). <https://doi.org/10.1029/2009GL039276>
- 1192 Moreno, M.; Melnick, D.; Rosenau, M.; Baez, J.; Klotz, J.; Oncken, O.; Tassara, A.; Chen, J.;
1193 Bataille, K.; Bevis, M.; Socquet, A.; Bolte, J.; Vigny, C.; Brooks, B.; Ryder, I.; Grund, V.;
1194 Smalley, B.; Carrizo, D.; Bartsch, M.; Hase, H. 2012. Toward understanding tectonic
1195 control on the Mw 8.8 2010 Maule Chile earthquake. *Earth and Planetary Science Letters*
1196 321-322: 152-165. <https://doi.org/10.1016/j.epsl.2012.01.006>
- 1197 Moreno, M.; Bedford, J.R.; Schurr, B.; Baez, J.C.; Urrutia, I.; Lange, D.; Oncken, O.; Melnick,
1198 D. 2016. From locking to coupling: Investigating the links between kinematics and stress
1199 accumulation along the Chilean subduction Zone. AGU Fall Meeting Abstracts, 2016.
- 1200 Mura, V.; Arancibia, G.; Browning, J.; Healy, D.; López-Contreras, C.; Morata, D.; Maza, S.;
1201 Cardona, C. 2025. Structural control on the Southern Andean Nevados de Chillán
1202 geothermal system. *Journal of Structural Geology* 196.
1203 <https://doi.org/10.1016/j.jsq.2025.105380>
- 1204 Niemeijer, A.; Di Toro, G.; Nielsen, S.; Di Felice, F. 2011. Frictional melting of gabbro under
1205 extreme experimental conditions of normal stress, acceleration, and sliding velocity.
1206 *Journal of Geophysical Research: Solid Earth* 116 (7): 1-18.
1207 <https://doi.org/10.1029/2010JB008181>
- 1208 Noda, H.; Lapusta, N. 2013. Stable creeping fault segments can become destructive as a
1209 result of dynamic weakening. *Nature* 493: 518-521. <https://doi.org/10.1038/nature11703>
- 1210 Olivar, J.; Nacif, S.; García, H.; Fennell, L.; Heit, B.; Folguera, A. 2022. Controls on crustal
1211 seismicity segmentation on a local scale in the Southern Central Andes. *Journal of South*
1212 *American Earth Sciences* 116: 103778. <https://doi.org/10.1016/j.jsames.2022.103778>

- 1213 Pardo-Casas, F.; Molnar, P. 1987. Relative motion of the Nazca (Farallon) and South
1214 American plates since late Cretaceous time. *Tectonics* 6 (3): 233-248.
1215 <https://doi.org/10.1029/TC006i003p00233>
- 1216 Pearce, R.K.; Sánchez de la Muela, A.; Moorkamp, M.; Hammond, J.O.S.; Mitchell, T.M.;
1217 Cembrano, J.; Araya Vargas, J.; Meredith, P.G.; Iturrieta, P.; Pérez-Estay, N.; Marshall,
1218 N.R.; Smith, J.; Yáñez, G.; Griffith, W.A.; Marquardt, C.; Stanton-Yonge, A.; Núñez, R.
1219 2020. Reactivation of fault systems by compartmentalized hydrothermal fluids in the
1220 Southern Andes revealed by magnetotelluric and seismic data. *Tectonics* 39:
1221 e2019TC005997. <https://doi.org/10.1029/2019TC005997>
- 1222 Pérez-Estay, N.; Yáñez, G.; Crempien, J.; Roquer, T.; Cembrano, J.; Valdenegro, P.;
1223 Aravena, D.; Arancibia, G.; Morata, D. 2020. Seismicity in a transpressional volcanic arc:
1224 The Liquiñe-Ofqui Fault System in the Puyuhuapi Area, Southern Andes, Chile (44°S).
1225 *Tectonics* 39: e2020TC006391. <https://doi.org/10.1029/2020TC006391>
- 1226 Pérez-Estay, M.; Ruz-Ginouves, J.; Pérez-Flores, P.; Sielfeld, G.; Roquer, T.; Cembrano, J.
1227 2023. Decoding the state of stress and fluid pathways along the Andean Southern
1228 Volcanic Zone. *Communications Earth & Environment* 4: 390.
1229 <https://doi.org/10.1038/s43247-023-01040-9>
- 1230 Pérez-Flores, P.; Cembrano, J.; Sánchez-Alfaro, P.; Veloso, E.; Arancibia, G.; Roquer, T.
1231 2016. Tectonics, magmatism and paleo-fluid distribution in a strike-slip setting: Insights
1232 from the northern termination of the Liquiñe-Ofqui fault System, Chile. *Tectonophysics*
1233 680: 192-210. <https://doi.org/10.1016/j.tecto.2016.05.016>
- 1234 Petit, J.P. 1987. Criteria for the sense of movement on fault surfaces in brittle rocks. *Journal*
1235 *of Structural Geology* 9 (5-6): 597-608. [https://doi.org/10.1016/0191-8141\(87\)90145-3](https://doi.org/10.1016/0191-8141(87)90145-3)
- 1236 Piquer, J.; Castelli, J.C.; Charrier, R.; Yáñez, G. 2010. The Cenozoic of the upper Teno
1237 River, Cordillera Principal, Central Chile: stratigraphy, plutonism and their relation with
1238 deep structures. *Andean Geology* 37 (1): 32-53. [http://dx.doi.org/10.5027/andgeoV37n1-](http://dx.doi.org/10.5027/andgeoV37n1-a2)
1239 [a2](http://dx.doi.org/10.5027/andgeoV37n1-a2)
- 1240 Piquer, J.; Skarmeta, J.; Cooke, D.R. 2015. Structural evolution of the Rio Blanco-Los
1241 Bronces District, Andes of Central Chile: controls on stratigraphy, magmatism, and
1242 mineralization. *Economic Geology* 110 (8): 1995-2023.
1243 <https://doi.org/10.2113/econgeo.110.8.1995>
- 1244 Piquer, J.; Rivera, O.; Yáñez, G.; Oyarzún, N. 2021. The Piuquencillo fault system: a long-
1245 lived, Andean-transverse fault system and its relationship with magmatic and
1246 hydrothermal activity. *Solid Earth* 12 (1): 253-273. <https://doi.org/10.5194/se-12-253-2021>
- 1247 Potin, B.; Ruiz, S.; Aden-Antoniow, F.; Madariaga, R.; Barrientos, S. 2025. A revised Chilean
1248 seismic catalog from 1982 to mid-2020. *Seismological Research Letters*, 96 (1): 484-498.
1249 <https://doi.org/10.1785/0220240047>

- 1250 Quiero, F.; Tassara, A.; Iaffaldano, G.; Rabbia, O. 2022. Growth of Neogene Andes linked to
1251 changes in plate convergence using high-resolution kinematic models. *Nature*
1252 *Communications* 13: 1339. <https://doi.org/10.1038/s41467-022-29055-4>
- 1253 Ramos, V. A.; Jordan, T. E.; Allmendinger, R. W.; Mpodozis, C.; Kay, S. M.; Cortés, J.M.;
1254 Palma, M. 1986. Paleozoic terranes of the central Argentine-Chilean Andes. *Tectonics*,
1255 5(6): 855-880. <https://doi.org/10.1029/TC005i006p00855>
- 1256 Rivera, O.; Cembrano, J. 2000. Modelo de formación de cuencas volcano-tectónicas en
1257 zonas de transferencia oblicuas a la cadena andina: El caso de las cuencas oligo-
1258 miocénicas de Chile central y su relación con estructuras NWW-NW (33°00'-34°30'S). In
1259 Congreso Geológico Chileno, No. 9, Actas 1:631-636. Puerto Varas, Chile.
- 1260 Rojas, C.; Beck Jr., M.E.; Burmester, R.F.; Cembrano, J.; Hervé, F. 1994. Paleomagnetism
1261 of the Mid-Tertiary Ayacura Formation, southern Chile: counterclockwise rotation in a
1262 dextral shear zone. *Journal of South American Earth Sciences* 7 (1): 45-56.
1263 [https://doi.org/10.1016/0895-9811\(94\)90033-7](https://doi.org/10.1016/0895-9811(94)90033-7)
- 1264 Rosenau, M.; Melnick, D.; Echtler, H. 2006. Kinematic constraints on intra-arc shear and
1265 strain partitioning in the southern Andes between 38°S and 42°S latitude. *Tectonics* 25
1266 (4): 1-16. <https://doi.org/10.1029/2005TC001943>
- 1267 Rousset, B. 2019. Months-long subduction slow slip events avoid the stress shadows of
1268 seismic asperities. *Journal of Geophysical Research: Solid Earth* 124 (7): 7337-7230.
1269 <https://doi.org/10.1029/2019JB018037>
- 1270 Rowe, C.D.; Griffith, W.A. 2015. Do faults preserve a record of seismic slip? A second
1271 opinion. *Journal of Structural Geology* 78: 1-26. <https://doi.org/10.1016/j.jsg.2015.06.006>
- 1272 Rowland, J.V.; Simmons, S.F. 2012. Hydrologic, magmatic, and tectonic controls on
1273 hydrothermal flow, Taupo Volcanic Zone, New Zealand: Implications for the formation of
1274 epithermal vein deposits. *Economic Geology* 107 (3): 427-457.
1275 <https://doi.org/10.2113/econgeo.107.3.427>
- 1276 Rutter, E.H. 1983. Pressure solution in nature, theory and experiment. *Journal of the*
1277 *Geological Society* 140 (5): 725-740. <https://doi.org/10.1144/gsjgs.140.5.0725>
- 1278 Ruz-Ginouvés, J.; Browning, J.; Cembrano, J.; Iturrieta, P.; Gerbault, M.; Sielfeld, G. 2020.
1279 Field observations and numerical models of a Pleistocene-Holocene feeder dyke swarm
1280 associated with a fissure complex to the east of the Tatara-San Pedro-Pellado complex,
1281 Southern Volcanic Zone, Chile. *Journal of Volcanology and Geothermal Research* 404.
1282 <https://doi.org/10.1016/j.jvolgeores.2020.107033>
- 1283 Sánchez, P.; Pérez-Flores, P.; Arancibia, G.; Cembrano, J.; Reich, M. 2013. Crustal
1284 deformation effects on the chemical evolution of geothermal systems-. The intra-arc
1285 Liquiñe-Ofqui fault system, Southern Andes. *International Geology Review* 55 (11): 1384-
1286 1400. <https://doi.org/10.1080/00206814.2013.775731>
- 1287 Santibañez, I.; Cembrano, J.; García-Pérez, T.; Costa, C.; Yáñez, G.; Marquardt, C.;
1288 Arancibia G.; González, G. 2019. Crustal faults in the Chilean Andes: geological

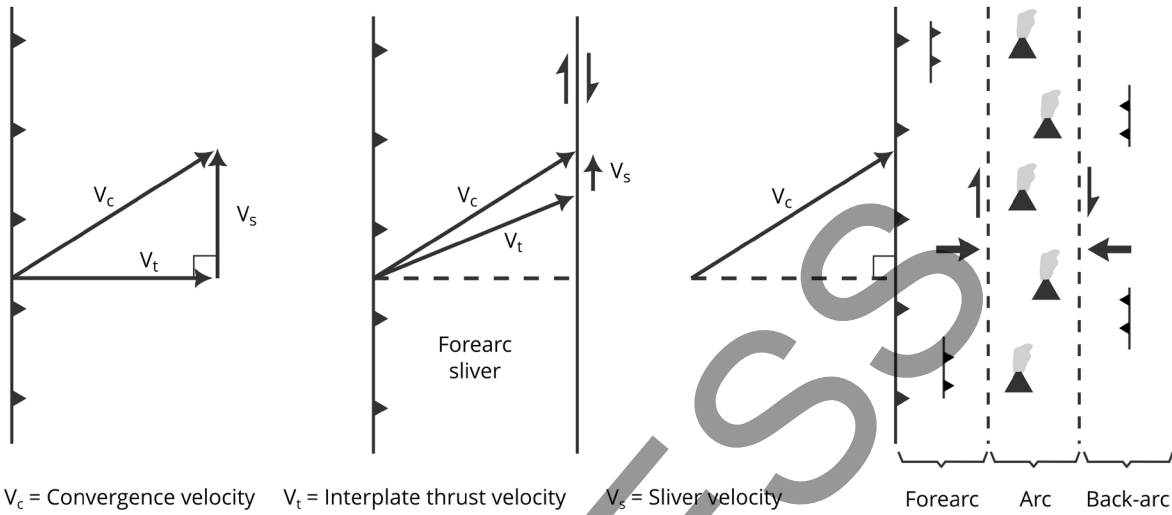
- 1289 constraints and seismic potential. *Andean Geology* 46 (1): 32-68.
1290 <http://dx.doi.org/10.5027/andgeoV46n1-3067>
- 1291 Savran, W. H.; Bayona, J. A.; Iturrieta, P.; Asim, K. M.; Bao, H.; Bayliss, K.; Herrmann, M.;
1292 Schorlemmer, D.; Marchling, P.J.; Werner, M.J. 2022. pyCSEP: A Python toolkit for
1293 earthquake forecast developers. *Seismological Society of America*, 93(5): 2858-2870.
1294 <https://doi.org/10.1785/0220220033>
- 1295 Seebeck, H.; Van Dissen, R.; Litchfield, N.; Barnes, P.M.; Nicol, A. Langridge, R.; Barrell,
1296 D.J.A.; Villamor, P.; Ellis, S.; Rattenbury, M.; Bannister, S.; Gerstenberger, M.; Ghisetti,
1297 F.; Sutherland, R.; Hirschberg, H.; Fraser, J.; Nodder, S.D.; Stirling, M.; Humphrey, J.;
1298 Bland, K.J.; Howell, A.; Mountjoy, J.; Moon, V.; Stahl, T.; Spinardi, F.; Townsend, D.;
1299 Clark, K.; Hamling, I.; Cox, S.; de Lange, W.; Wopereis, P.; Johnston, M.; Morgenstern,
1300 R.; Coffey, G.; Eccles, J.D.; Little, T.; Fry, B.; Griffin, J.; Townend, J.; Mortimer, N.;
1301 Alcaraz, S.; Massiot, C.; Rowland, J.V.; Muirhead, J.; Upton, P.; Lee, J. 2023. The New
1302 Zealand Community Fault Model–version 1.0: An improved geological foundation for
1303 seismic hazard modelling. *New Zealand Journal of Geology and Geophysics* 67 (2): 209-
1304 229. <https://doi.org/10.1080/00288306.2023.2181362>
- 1305 Sernageomin. 2003. Mapa Geológico de Chile: versión digital. Servicio Nacional de
1306 Geología y Minería, Publicación Geológica Digital No. 4 (CD-ROM, versión 1.0, 2003).
1307 Santiago, Chile.
- 1308 Sielfeld, G.; Cembrano, J.; Lara, L. 2017. Transtension driving volcano-edifice anatomy:
1309 Insights from Andean transverse-to-the-orogen tectonic domains. *Quaternary*
1310 *International* 438: 33-49. <https://doi.org/10.1016/j.quaint.2016.01.002>
- 1311 Sielfeld, G.; Lange, D.; Cembrano, J. 2019a. Intra-arc crustal seismicity: Seismotectonic
1312 implications for the Southern Andes Volcanic Zone, Chile. *Tectonics* 38: 552-578.
1313 <https://doi.org/10.1029/2018TC004985>
- 1314 Sielfeld, G.; Ruz, J.; Brogi, A.; Cembrano, J.; Stanton-Yonge, A.; Pérez-Flores, P.; Iturrieta,
1315 P. 2019b. Oblique-slip tectonics in an active volcanic chain: A case study from the
1316 Southern Andes. *Tectonophysics* 770. <https://doi.org/10.1016/j.tecto.2019.228221>
- 1317 Somoza, R. 1998. Updated Nazca (Farallon) – South America relative motions during the
1318 last 40 My: implications for mountain building in the central Andean region. *Journal of*
1319 *South American Sciences* 11 (3): 211-215. [https://doi.org/10.1016/S0895-9811\(98\)00012-1](https://doi.org/10.1016/S0895-9811(98)00012-1)
1320 [1](https://doi.org/10.1016/S0895-9811(98)00012-1)
- 1321 Stanton-Yonge, A.; Griffith, W.A.; Cembrano, J.; St. Julien, R.; Iturrieta, P. 2016. Tectonic
1322 role of margin-parallel and margin-transverse faults during oblique subduction in the
1323 Southern Volcanic Zone of the Andes: Insights from Boundary Element Modeling.
1324 *Tectonics* 35: 1990-2013. <https://doi.org/10.1002/2016TC004226>
- 1325 Stanton-Yonge, A.; Sánchez de la Muela, A.; Pearce, R.K.; Hammond, J.O.S.; Mitchell,
1326 T.M.; Hicks, S.P.; Griffith, W.A.; Moorkamp, M.; Meredith, P.; Cembrano, J. 2025. Fluid
1327 pressure fluctuations and the seismic signature of a fault-controlled fluid migration pulse.
1328 *Earth and Planetary Science Letters* 662. <https://doi.org/10.1016/j.epsl.2025.119388>

- 1329 Stern, C.R.; Skewes, M.A.; Arévalo, A. 2011. Magmatic evolution of the giant El Teniente
1330 Cu-Mo Deposit, Central Chile. *Journal of Petrology* 52 (7-8): 1591-1617.
1331 <https://doi.org/10.1093/petrology/eqq029>
- 1332 Tapia, F.; Farías, M.; Naipauer, M.; Puratich, J. 2015. Late Cenozoic contractional evolution
1333 of the current arc-volcanic region along the southern Central Andes (35°20'S). *Journal of*
1334 *Geodynamics* 88: 36–51. <https://doi.org/10.1016/j.jog.2015.01.001>
- 1335 Tassara, A.; Yáñez, G. 2003. Relación entre el espesor elástico de la litósfera y la
1336 segmentación tectónica del margen andino (15-47°S). *Andean Geology* 30 (2): 159-186.
1337 <http://dx.doi.org/10.4067/S0716-02082003000200002>
- 1338 Teyssier, C.; Tikoff, B.; Markley, M. 1995. Oblique plate motion and continental tectonics.
1339 *Geology* 23 (5): 447-450. [https://doi.org/10.1130/0091-](https://doi.org/10.1130/0091-7613(1995)023%3C0447:OPMACT%3E2.3.CO;2)
1340 [7613\(1995\)023%3C0447:OPMACT%3E2.3.CO;2](https://doi.org/10.1130/0091-7613(1995)023%3C0447:OPMACT%3E2.3.CO;2)
- 1341 Thompson, S.N. 2002. Late Cenozoic geomorphic and tectonic evolution of the Patagonian
1342 Andes between latitudes 42°S and 46°S: An appraisal based on fission-track results from
1343 the transpressional intra-arc Liquiñe-Ofqui fault zone. *GSA Bulletin* 114 (9): 1159-1173.
1344 [https://doi.org/10.1130/0016-7606\(2002\)114%3C1159](https://doi.org/10.1130/0016-7606(2002)114%3C1159)
- 1345 U.S. Geological Survey (USGS). 2017. Advanced National Seismic System (ANSS)
1346 Comprehensive Earthquake Catalog. <https://earthquake.usgs.gov/data/comcat/>
- 1347 Vega-Ruiz, A.; Cortés-Aranda, J.; Aguilera-Cortés, R.; Astudillo-Sotomayor, L.; Riedel, M.;
1348 Espinoza, M.; Tassara, A.; Nelson, A.; Melnick, D.; Lupi, M.; Arriagada, S.; Spúlveda, T.;
1349 Álvarez-Amado, F.; Navarro, L. 2025. Pliocene to Holocene deformation and earthquake
1350 potential of the Mesamávida Fault, West Andean Thrust System of Central-Southern
1351 Chile (36° S). *Tectonics* 44 (7): e2025TC008848. <https://doi.org/10.31223/X5T153>
- 1352 Vargas, G.; Klinger, Y.; Rockwell, T.K.; Forman, S.L.; Rebolledo, S.; Baize, S.; Lacassin, R.;
1353 Armijo, R. 2014. Probing large intraplate earthquakes at the west flank of the Andes.
1354 *Geology* 42 (12): 1083-1086. <https://doi.org/10.1130/G35741.1>
- 1355 Vigide, N.; Olivar, J.; Mescua, J.; Basualto, D.; Farías, C.; Tassara, A.; García, S. 2025. A
1356 transpressive stress regime for the Laguna del Maule Volcanic Complex. *Journal of South*
1357 *American Earth Sciences* 161: 105563. <https://doi.org/10.1016/j.jsames.2025.105563>
- 1358 Vigny, C.; Socquet, A.; Peyrat, S.; Ruegg, J.C.; Métois, M.; Madariaga, R.; Morvan, S.;
1359 Lancieri, M.; Lacassin, R.; Campos, J.; Carrizo, D.; Bejar-Pizarro, M.; Barrientos, S.;
1360 Armijo, R.; Aranda, C.; Valderas-Bermejo, M.-C.; Ortega, I.; Bondoux, F.; Baize, S.; Lyon-
1361 Caen, H.; Pavez, A.; Vilotte, J.P.; Bevis, M.; Brooks, B.; Smalley, R.; Parra, H.; Baez, J.-
1362 C.; Blanco, M.; Cimbaro, S.; Kendrick, E. 2011. The 2010 Mw 8.8 Maule Megathrust
1363 earthquake of Central Chile, monitored by GPS. *Science* 332 (6036): 1417-1421.
1364 <https://doi.org/10.1126/science.1204132>
- 1365 Wall R.; Gana, P.; Gutiérrez, A. 1996. Mapa geológico del área de San Antonio-Melipilla,
1366 regiones de Valparaíso, Metropolitana y del Libertador General Bernardo O'Higgins.

- 1367 Servicio Nacional de Geología y Minería, Mapas Geológicos N°2, escala 1:100.000, 1
1368 mapa, 1 anexo.
- 1369 Wang, K.; Hu, Y.; Bevis, M.; Kendrick, E.; Smalley Jr., R.; Barriga Vargas, R.; Lauría, E.
1370 2007. Crustal motion in the zone of the 1960 Chile earthquake: Detangling earthquake-
1371 cycle deformation and forearc-silver translation. *Geochemistry, Geophysics, Geosystems*
1372 8 (10): 1-14. <https://doi.org/10.1029/2007GC001721>
- 1373 Weatherill, G. A.; Pagani, M.; Garcia, J. 2016. Exploring earthquake databases for the
1374 creation of magnitude-homogeneous catalogues: tools for application on a regional and
1375 global scale. *Geophysical Journal International* 206.3: 1652-1676.
1376 <https://doi.org/10.1093/gji/ggw232>
- 1377 Weller, O.; Lange, D.; Tilmann, F.; Natawidjaja, D.; Rietbrock, A.; Collings, R.; Gregory, L.
1378 2012. The structure of the Sumatran Fault revealed by local seismicity. *Geophysical*
1379 *Research Letters* 39 (1): 1-7. <https://doi.org/10.1029/2011GL050440>
- 1380 Yáñez, G.A.; Gana, P.; Fernández, R. 1998. Origen y significado geológico de la Anomalía
1381 Melipilla, Chile central. *Revista Geológica de Chile* 25 (2): 175-198.
1382 <http://dx.doi.org/10.4067/S0716-02081998000200005>
- 1383 Yáñez, G.; Pérez-Estay, N.; Araya-Vargas, J.; Sanhueza, J.; Figueroa, R.; Maringue, J.;
1384 Rojas, T. 2020. Shallow anatomy of the San Ramón Fault (Chile) constrained by
1385 geophysical methods: Implications for its role in the Andean deformation. *Tectonics* 39
1386 (8): 1-21. <https://doi.org/10.1029/2020TC006294>
- 1387 Yáñez, G.; Piquer, J.; Rivera, O. 2024. On the role of trans-lithospheric faults in the long-
1388 term seismotectonic segmentation of active margins: a case study in the Andes.
1389 *European Geosciences Union* 15 (11): 1319-1342. [https://doi.org/10.5194/se-15-1319-](https://doi.org/10.5194/se-15-1319-2024)
1390 [2024](https://doi.org/10.5194/se-15-1319-2024)
- 1391 Youngs, R.; Coppersmith, K. 1985. Implications of fault slip rates and earthquake recurrence
1392 models to probabilistic seismic hazard estimates. *Bulletin of the Seismological Society of*
1393 *America* 75 (4): 939-964. [https://doi.org/10.1016/0148-9062\(86\)90651-0](https://doi.org/10.1016/0148-9062(86)90651-0)
- 1394

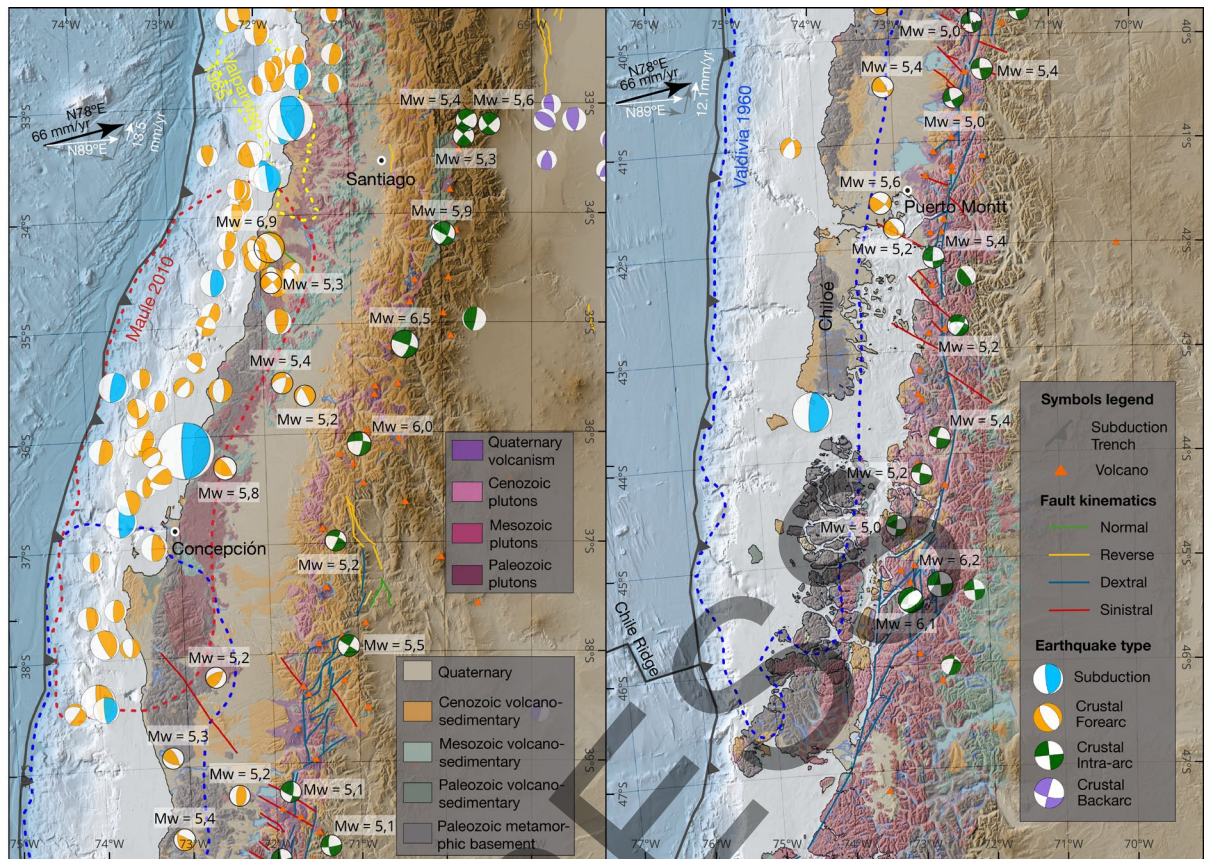
1395 **Figure Captions**

A Complete partitioning (Fitch, 1972) **B** Partial partitioning (Beck, 1991 and McCaffrey, 1992) **C** Transpressional magmatic arc (de Saint Blanquat *et al.*, 1998)



1396

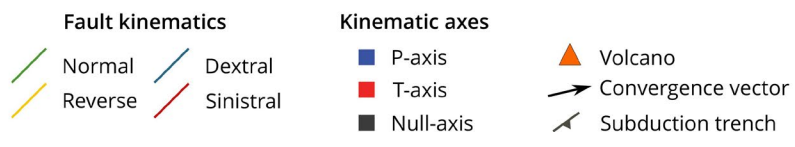
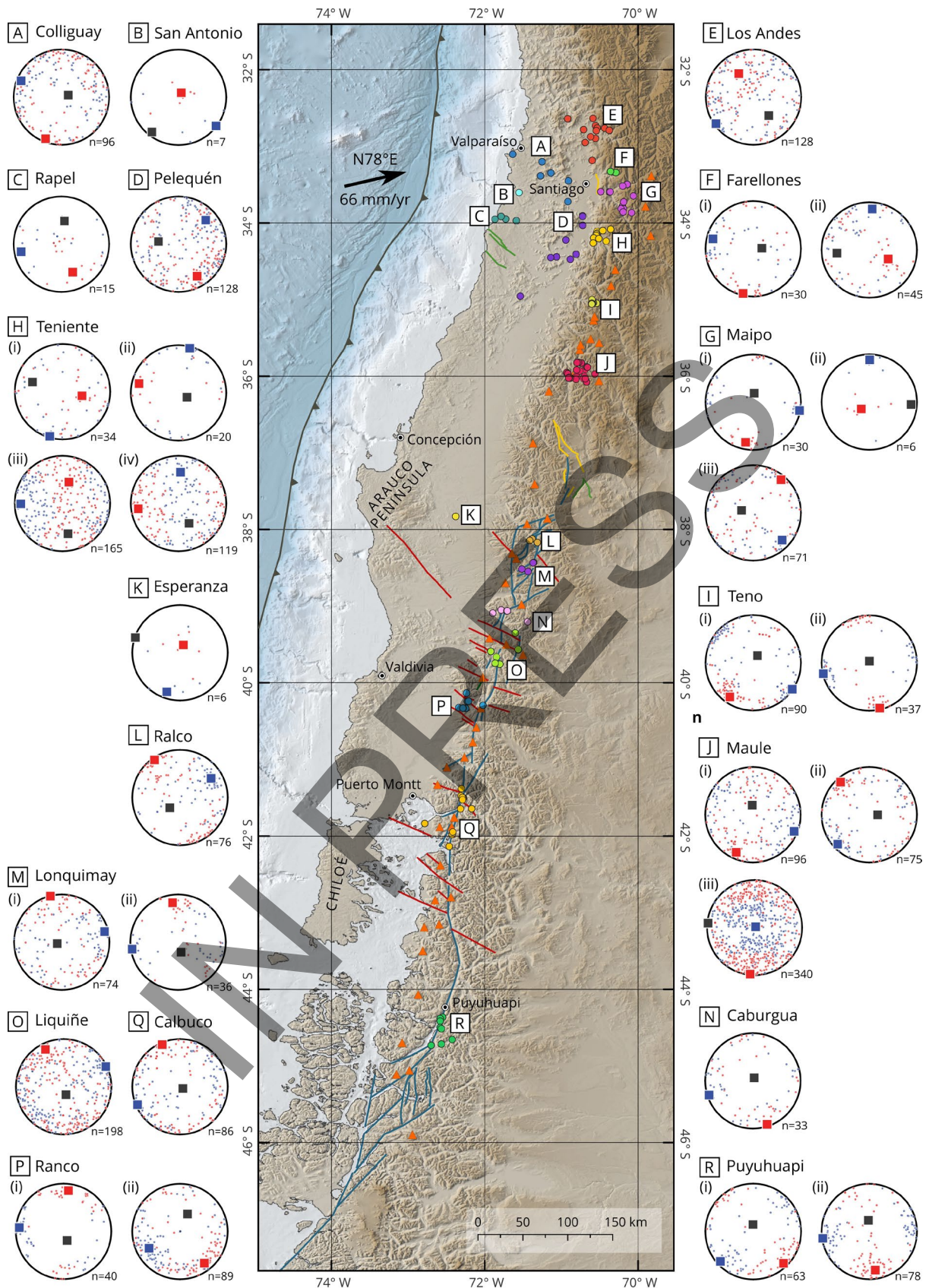
1397 ● **Fig. 1.** Schematic diagram illustrating the evolution of the slip partitioning concept
 1398 over the past five decades. **A.** Complete partitioning of the convergence slip
 1399 vector (Fitch, 1972). **B.** Partial partitioning (e.g., Beck, 1991; McCaffrey, 1992). **C.**
 1400 Slip partitioning considering a transpressional magmatic arc domain (de Saint
 1401 Blanquat *et al.*, 1998).



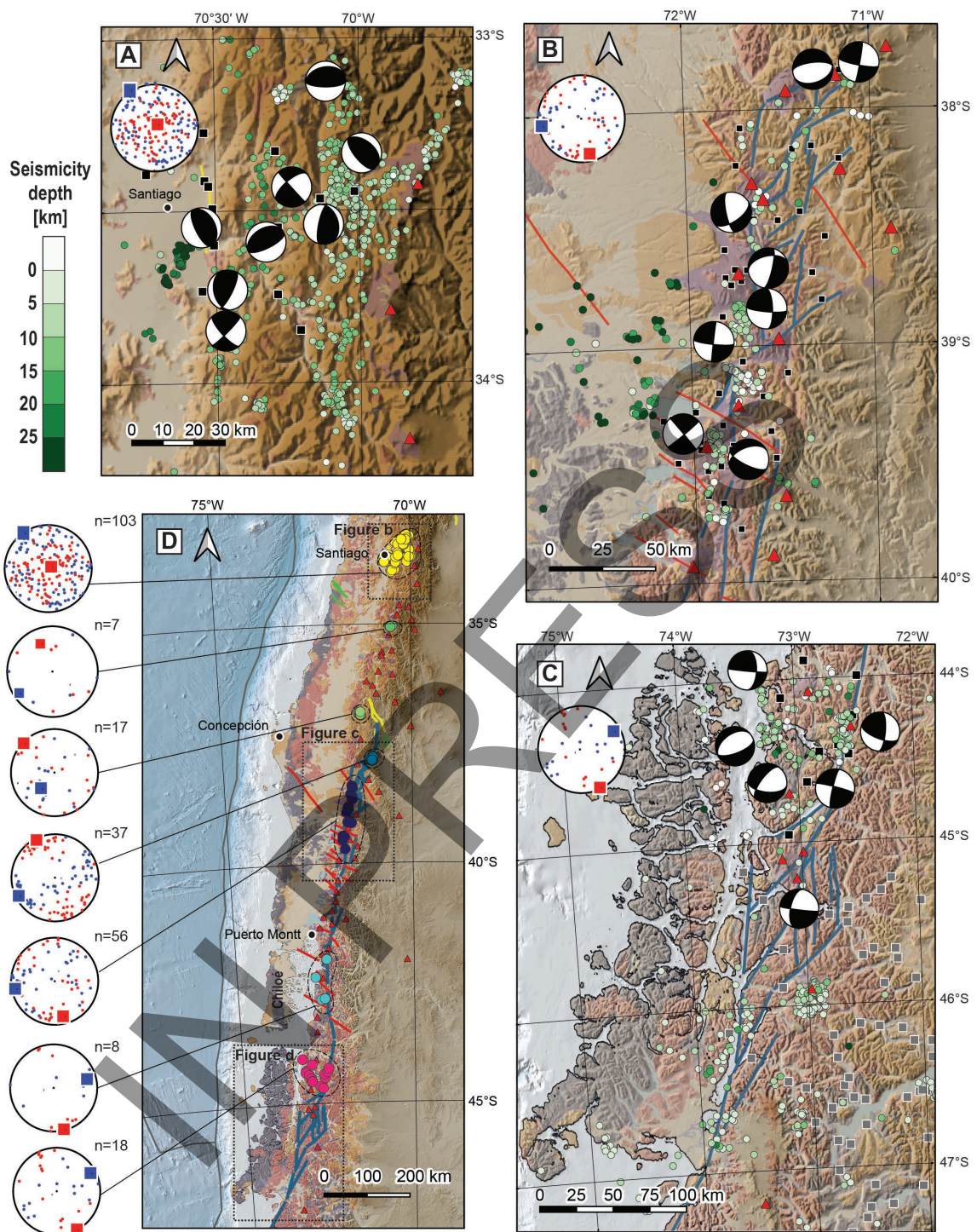
1402 ●

1403 ● **Fig. 2.** Tectonic, geological, and seismological setting of the Chilean Andes
 1404 between 33° and 47° S, mainly based on Sernageomin (2003), Cembrano and
 1405 Lara (2009), Tapia et al. (2015), Stanton-Yonge et al. (2016), Sielfeld et al.
 1406 (2019a), and Olivar et al. (2022). Main Quaternary crustal faults (data from
 1407 Santibáñez et al., 2019 and Costa et al., 2020), and Holocene volcanoes are
 1408 included for reference. Crustal seismicity in the overriding plate is shown for
 1409 earthquakes with $M_w > 5.0$ based on data from global networks. Selection
 1410 subduction interface events (Stanton-Yonge et al., 2016) are displayed alongside
 1411 crustal seismicity. The segmented blue line indicates the rupture zone of the Mw
 1412 9.5 1960 Valdivia earthquake (Moreno et al., 2009), the red segmented line
 1413 marks the Mw 8.8 2010 Maule earthquake (Moreno et al., 2012), and the yellow
 1414 segmented line shows the Mw 8.0 1985 Valparaíso earthquake (Bravo et al.,
 1415 2019). The partitioning of the convergence vector (N78°E, black arrow) into its

1416 margin-parallel and margin-orthogonal (grey arrows) components is depicted for
1417 the regions between 34° and 38° S (where the margin trends N20°E), and
1418 between 38° and 47° S (where the margin trends N10°E). The average slip vector
1419 of subduction earthquakes (N89°E; Stanton-Yonge et al., 2016) is also shown
1420 (white arrow in between the convergence vector and the orthogonal to the
1421 trench), illustrating the partial partitioning of convergence along the margin. The
1422 residual margin-parallel component to be accommodated within the overriding
1423 plate is indicated for both regions (white arrows parallel to the plate margin; 13.5
1424 mm/year for 34°–38° S and 12.1 mm/year for 38°–47° S). The full classified
1425 catalog and the P- and T-axes for each earthquake class are shown respectively
1426 in figures S1 and S2 in the Supplementary Material. See the Data and Resources
1427 chapter for more information on data source compilation and processing.



1429 ● **Fig. 3.** Compilation and analysis of both published (e.g., Arancibia et al., 1999;
1430 Lavenu and Cembrano, 1999; Pérez-Flores et al., 2016; Roquer et al., 2022) and
1431 new (this study) fault slip data. Structural sites, or combinations of them, are
1432 grouped in clusters in case of consistent P–T results (labelled A to R). On the
1433 map, each structural site is shown as a circle, colored by cluster group. Clusters
1434 with more than one distinct solution are displayed with multiple lower-hemisphere
1435 equal-area stereonet, labeled i to iv, depending on the number of additional
1436 solutions. All clusters show both the distribution of P and T instantaneous strain
1437 axis orientations for all individual faults (blue and red dots), as well as the
1438 kinematic axes for the fault population, calculated using the methods established
1439 after Marret and Allmendinger (1990) and Allmendinger et al. (2012). The
1440 maximum shortening axis (P), minimum shortening axis (T), and the null axis are
1441 represented as blue, red, and black squares, respectively. Red triangles
1442 represent active volcanoes.

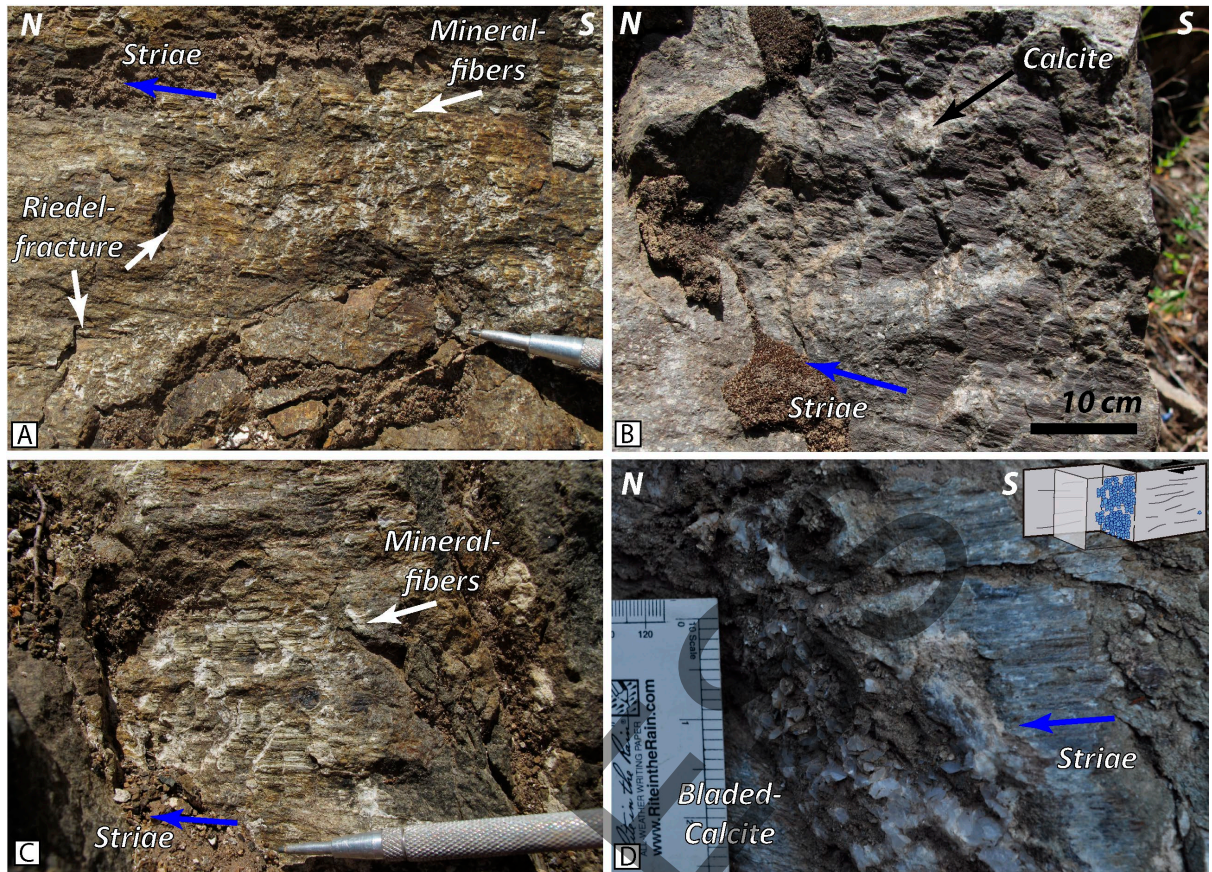


1443 ●

1444 ● **Fig. 4.** Compilation and analysis of published crustal seismicity and a subset of
 1445 focal mechanisms from local seismic networks, including events with $M_w < 5.0$.

1446 Black and gray squares mark seismic stations from temporary local network

1447 deployments in previous studies, from which the data were compiled. Panels **(A)**,
1448 **(B)**, and **(C)** show insets with previously published seismicity for the Maipo,
1449 Araucanía, and Aysén regions, respectively. The Maipo region includes
1450 seismicity and focal mechanisms from Ammirati et al. (2019). The Araucanía
1451 region exhibits seismicity reported by Sielfeld et al. (2019a), along with focal
1452 mechanisms from the same authors and from Montenegro et al. (2021). The
1453 Aysén region shows seismicity reported by Agurto et al. (2014) and Pérez-Estay
1454 et al. (2020), accompanied by focal mechanisms from Mora et al. (2010) and
1455 Pérez-Estay et al. (2020), the latter referring to the initial state of the 2007 Aysén
1456 crisis. Panel **(D)** shows a regional map with the locations of individual seismic
1457 events (colored circles) for which focal mechanism solutions were obtained from
1458 different local seismic networks. Each local network is represented by a distinct
1459 color. Background geology and structures are as shown in figure 2. The stereonet
1460 plots summarize the P- and T-axis orientations of all mechanisms recovered by
1461 each local network, with blue and red squares indicating the average P- and T-
1462 axis directions for each network, respectively. For more information, the reader is
1463 referred to the literature cited in this study and to the Data and Resources
1464 chapter.



1465

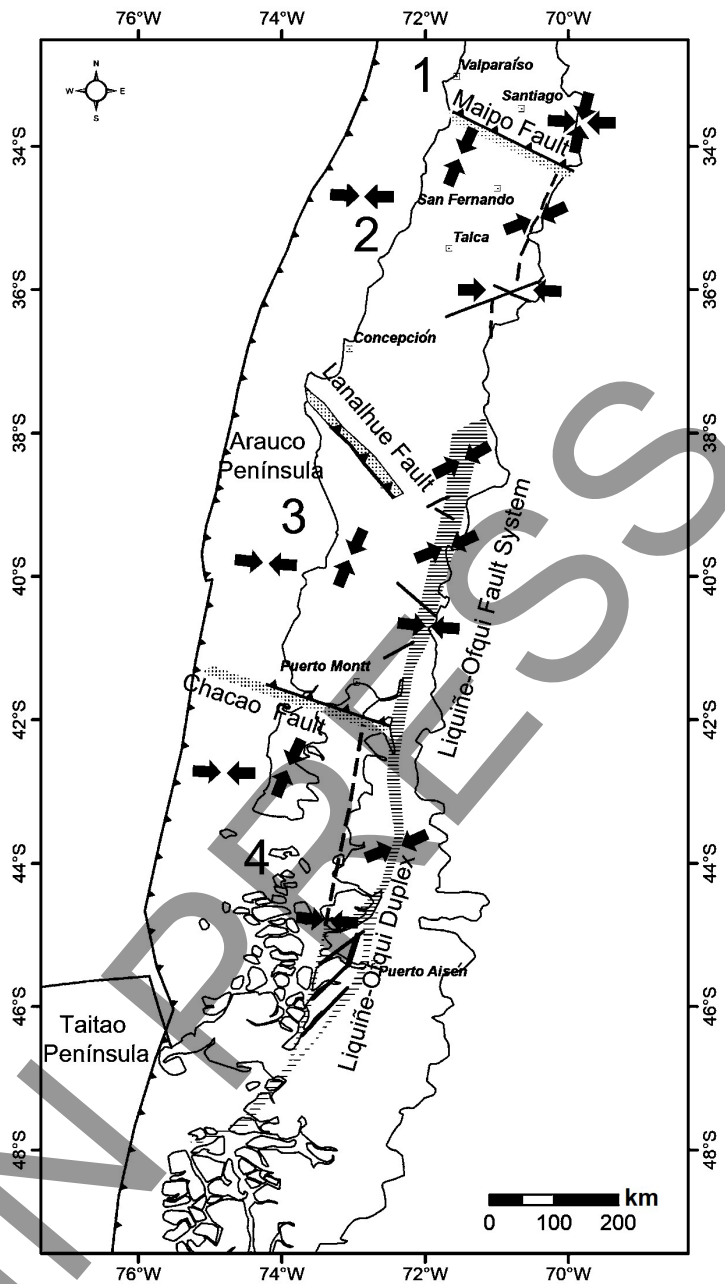


1466



Fig. 5. Typical examples of mesoscopic fault surfaces with striae (slickensides) in the study area. These surfaces exhibit one or more of the following features: (A) dextral Riedel-type fractures and mineral fibers; (B) calcite precipitation behind fault steps; (C) zeolite slickenfibers; and (D) bladed-like calcite inside a dilatational jog (diagram provided for spatial context).

1470



1471 ●

1472 ● **Fig. 6.** Summary cartoon illustrating the along- and across-strike segmentation in
 1473 the geometry and kinematics of slip and deformation partitioning in the Southern
 1474 Andes. All segments are bounded by south-verging, WNW- to NW-striking
 1475 reverse faults/deformation zones, namely Maipo, Llanalhue, and Chacao. Black
 1476 arrows roughly indicate approximate P directions (T axes are not shown for

1477 simplicity). The dotted patterns around the major segment boundary faults
1478 represent their approximate widths as deformation zones. The striped pattern
1479 associated with the LOFS marks the approximate region containing both master
1480 and subsidiary faults. See text for details.

IN PRESS